Journal of Molecular Liquids 288 (2019) 111006

Contents lists available at ScienceDirect

Journal of Molecular Liquids

journal homepage: www.elsevier.com/locate/molliq

Morphology control synthesis of iron-rich Sinai clay by novel O, N, S-heterocyclic moieties: Magnetic organoclays for various strategic uses in lubricating oilfield industry

Sarah A. Abdel-Latef [a], Atef S. Darwish [a,*], Sameh A. Rizk [a], Sayed K. Atya [b], Maher H.E. Helal [c]

[a] Department of Chemistry, Faculty of Science, Ain Shams University, 11566 Cairo, Egypt
[b] Egyptian Petroleum Research Institute, Evaluation and Analysis Department, 1 Ahmed El-Zomor Street, Nasr City, 11727 Cairo, Egypt
[c] Department of Chemistry, Faculty of Science, Helwan University, Cairo, Egypt

ARTICLE INFO

Article history:
Received 5 March 2019
Received in revised form 2 May 2019
Accepted 19 May 2019
Available online 24 May 2019

Keywords:
Iron-rich clay
Organoclay
Waste lubricant oil
Regenerated oil
Acid production

ABSTRACT

Herein, iron-rich Sinai clay (ATT) was chemically-modified by inventive azacoumarin (Az), spiropyrrolidine (Sp) and imidazothiadiazole (Im) compounds forming clay-containing hematite particles. Interplay between the chemistry of organo-compounds and the clay-sheet structure was interpreted by running DFT-calculations and physicochemical studies (XRD, FTIR, DLS, HR-TEM, N_2-physisorption and magnetic analyses). The planar/nucleophilic Az-molecules preferentially occupied clay interlayer-spacings and weaken the combination between silicate-layers, forming large-sizes of completely intercalated clay layers of mesoporous structure with poor physicochemical properties. Besides, angstrom-size hematite particles (<20 Å) appeared in these spacings. The non-planar/electrophilic Sp-molecules promptly attack silicate-layers to form low-sized fully exfoliated clay particles with micro/meso- porous structure of developed magnetic and physicochemical properties. The planar Im-molecules of nucleophilic/electrophilic character enthused construction of intercalated/exfoliated clay system over which magnetic hematite-nanospheres (~10 nm) were splattered. A road ahead to setting-up these organoclays in lubricant-oil industry was planned. Magnetic Sp/ATT organoclay was promisingly behaving as base-oil lubricant additive of increased-efficiency (164%) to oil electrical property. Magnetic Im/ATT organoclay was candidate for being an easily-separable waste-oil regeneration agent, while Az/ATT was highlighted as efficient catalyst for acetic-acid production from waste-lubricant-oil (45% yield). Future studies to applicability of iron-rich organoclays in lubricant-oil industry are optimistic and withstand overwhelmingly positive thus far.

1. Introduction

Clays are ubiquitous in nature, with nanoscopic size, anisotropic shape, nontoxic nature, and low cost. However, the efficient use of clays is restricted by their low porosity and limited morphological stability [1,2]. The most common complaint about clays is the diversity of the nature of active sites in clay layers such as silanols, aluminols, interlamellar cations and physisorbed water [3,4]. These sites create various interacting entities, e.g. coulombic forces and hydrogen bonds that are capable to customize stacked and stiff clay platelets with straiten interlayered spaces [5,6].

Special attention was paid to mollify the interaction between clay platelets and to widen the gaps in between, looking for upgrading the adsorptive, magnetic, electrical, mechanical and catalytic properties of clays [7–12]. Among the interesting approaches used for these reasons, inoculation of bulk inorganic polyoxocations as well organic macromolecules within the clay interlayer-spaces had received the greatest importance [8–15]. An important member of polyoxocations, iron oxide species possessed an excellent affinity to be easily separated from any medium by a simple magnetic process [16]. The availability of natural clays to be functioned as excellent cation exchangers stimulated insertion of copious amounts of iron oxides into their interlamellar spaces, following so-called pillaring process [8]. Unfortunately, efficient use of pillared clays was limited by presence of rigid and non-parallel ordered clay platelets of lower aluminum content in their octahedral sheets, displaying extremely acidic clays of poor swellable behavior [8,13]. A way to refrain the flaws in pillaring method, very few researches dealt with proceeding natural containing iron-clays instead of iron oxide-pillared ones for industrial applications [1,12]. On the other hand, modifying the clay sheets by surfactants seemed to face drawbacks resulting from the limited number of chelating agents in these molecules, which, in turn, failed to draw the whole molecule to the interlayer surfaces of clay [14,15]. Like wisely, modifying clay lamellae by polymeric species

* Corresponding author.
E-mail address: atef_mouharam@sci.asu.edu.eg (A.S. Darwish).

https://doi.org/10.1016/j.molliq.2019.111006
0167-7322/

was ebbed somewhat recently because of the complex misinterpreted interactions between them, as the various formed structural entities are found to behave differently [3–5].

In the two last decades, heterocyclic compounds had received enormous attention as core components for pharmaceutical industry [17–24]. Among the extensive researches to the pharmacological application of O, N, S-heterocyclic moieties, azacoumarin, spiropyrrolidine and imidazothiadiazole derivatives appeared as drug candidates of highly efficient antimicrobial [17–19], antioxidant [20–22] and anticancer [17,23,24] activities. Foregoing studies in the biomedical behavior of substituted imidazothiadiazole compounds afforded very promising future for their use as antitubercular and antihyperlipidemic agents, and apoptosis inducers in tumor cells [25–27]. Moreover, applications to imidazothiadiazole compounds were recently extended to cover the industrial field, whereas the azacoumarin derivatives showed high responsiveness to be employed as photo-switchable coatings with pronounced electro-optical properties and the spiropyrrolidine compounds were promisingly used in development of dye-sensitized solar cell [28–30]. To the best of our knowledge, dealing with O, N, S-heterocyclic moieties as organo-modifiers to the lamellar structure of clay has not been reported yet.

Engine oil is an important lubricant that is used in automobiles for protecting motors from expectable damages and energy consumptions [31,32]. Unfortunately, hastening development in engine technology arouse serious imperfections about the affinity of engine oil to safe machineries from high frictions and lubricants' durability [32]. In a study conducted in 2012 by Holmberg et al. [33], it was concluded that more than one third of energy from fuel is wasted by frictional losses from engines and other moving parts such as brakes, and tires. In this respect, ameliorating the electrical properties of engine lubricant oil to minimize frictions - in other words, improving friction resistance and anti-wear character of lubricant oil, had received worthy attentions in the last few years being an urgent requisite in the context of consuming energy loss and protecting machineries from highly probable damages [34,35]. Moreover, deficiency of adequate supplies of base oil stimulated the scientific community into looking for the possibility of either regenerating and/or producing highly acidic solutions from lubricating oil wastes to afford the world's demand for energy and sustainability [31,36–38]. Among the diverse approaches for oil recycling, fewer studies dealt only with acid-activated clays as auspicious adsorbents for production of regenerated lubricant oil [31,36].

In view of the considerations presented above, the present work is an unparalleled-wide study of two main objectives. First, is to invent new route for clay modification based on using natural containing iron-clay (Sinai clay) and less lipophilic O, N, S-heterocyclic moieties to customize organoclay containing hematite (α-Fe_2O_3) particles, where heterocyclic moieties invade clay interlamellar spaces adopting distinct and interpreted interacting modes with both clay platelets and low-sized magnetic species (α-Fe_2O_3). Second, is to manage these magnetic organoclays in lubricating oil industry through examining them as additives to enhance electrical and lubricity properties of base oil, agents to regenerate waste lubricating oil, and oxidative catalysts for acid production from waste lubricant oil.

2. Experimental

2.1. Materials

The (E)-3-(2-hydroxyphenyl)-1-(naphthalene-2-yl) prop-2-en-1-one compound derived from chalcones was procured from Sigma-Aldrich chemical Co. Germany. Ethyl cyanoacetate, ammonium acetate, β-pyrollidone-ethanol, sarcosine, 2-amino-5-styryl-1,3,4-thiazole, triethyl amine (TEA) and hydrogen peroxide were supplied by Riedel-de Haën chemical Co. Germany. The naturally iron-rich clay was collected from Saint Catharine valley, Sinai, Egypt. This clay was dried at 100 °C for 5 h, ground and sieved to obtain a fraction of 20–40 μm. The main characterization aspects of this natural clay were measured and depicted as follows: (i) cation exchange capacity (CEC) = 76 meq/100 g, (ii) surface area = 135 $m^2\ g^{-1}$, and (iii) mineralogical chemical composition (mass %): SiO_2, 50.29; Al_2O_3, 19.37; Fe_2O_3, 11.38; Na_2O, 2.81; CaO, 1.21; MgO, 1.09; K_2O, 0.89; TiO_2, 0.46. The recorded iron level in Sinai clay placed it as one of the most discovered iron-rich clay, being stand in competition with the produced clays by Asian companies [39–41]. All other chemicals were of analytical grade from Merck and were used without further purification.

2.2. Characterization and computational methods of O, N, S-heterocyclic moieties

The melting points were measured with a Gallenkamp melting point apparatus (MFB 595–0366). The IR spectra were recorded on a Pye-Unicam SP-3-300 infrared spectrophotometer (KBr Pellets) and expressed in wave number (cm^{-1}). ^{1}H NMR spectrometry was performed via Bruker spectrophotometer at 400 MHz using TMS as internal standard with residual signal ($\delta = 2.51$ ppm) of the deuterated solvent (DMSO-d_6). ^{13}C NMR spectra were recorded on the Varian Mercury VX-300 spectrometer at 125 MHz. Chemical shifts (δ) were quoted in ppm. The abbreviations used were as follows: s, singlet; d, doublet; m, multiplet. All coupling constant (J) values were given in hertz. The molecular weight of the obtained heterocyclic compounds was supported by mass spectrometer (GCMS-QP-1000EX, Shimadzu, Middle East Branch Dubai) at 70 eV. Elemental analyses of all compounds were also performed on CHN analyzer within theoretical values of ±0.1–0.4%. The obtained spectra were presented as supplementary materials (Fig. S1-S3).

Computational studies for all synthesized heterocyclic compounds were carried out using Materials Studio 6.0 (MS 6.0) software from Accelrys, Inc. DMol3 module was used to perform the density functional theory (DFT) calculations using Perdew and Wang LDA exchange-correlation functional and DND basis set. The DFT calculated parameters involved electron density (ω), dipole moment (μ) and hydration energy (E_H), and Frontier molecular orbitals including the highest occupied molecular orbitals (HOMOs) as well the lowest unoccupied molecular orbitals (LUMOs) [42].

2.3. Synthetic procedures and structure confirmations of O, N, S-heterocyclic moieties

The synthetic scheme (Fig. 1) illustrated using (E)-3-(2-hydroxyphenyl)-1-(naphthalene-2-yl)prop-2-en-1-one chalcone derivative compound as a main precursor for preparing various O, N, S-heterocyclic compounds following three alternative procedures.

For the first procedure (*route I*), substituted azacoumarin, which IUPAC name was 4-amino-5-(2-hydroxyphenyl)-7-(naphthalen-2-yl)-2-oxo-2H-pyrano[2,3-*b*]pyridine-3-carbonitrile), was prepared adopting ultrasonic-assisted method [43]. Chalcone (0.05 mol), ethyl cyanoacetate (0.05 mol) and ammonium acetate (0.04 mol) were grinded together in a mortar, then the whole mixture was transferred into a 250 mL round bottom flask with the addition of 5 mL ethanol. The reaction mixture was then ultrasonicated at 30 °C. The reaction progression was monitored by thin layer chromatography (TLC) using ethyl acetate/benzene mixture (1:19 v/v) as solvent system. Sonication was continued until the chalcone disappeared as indicated by TLC. A solid product was obtained within 20 to 25 min of irradiation. Afterwards, the mixture was poured into crushed ice with constant stirring to obtain a yellow solid mass, which was dried and fractionally crystallized from 95% ethanol, and allocated by "Az".

Yield (88%); Yellow crystal; m.p. 170–172 °C. FTIR spectrum (Fig. S1, a) showed absorption band (in cm^{-1}) at: 3467 (OH), 3284, 3180)NH_2), 3042 (CH aromatic), 1582 (CN), 1743 (CO lactone). ^{1}H NMR spectrum (Fig. S1, b) presented signals (δ) in ppm at: 2.54 (s, 2H, NH_2), 7.72 (s, 1H, CH═, arylidene in form of *E*-configuration), 7.78 (s, 1H, CH═,

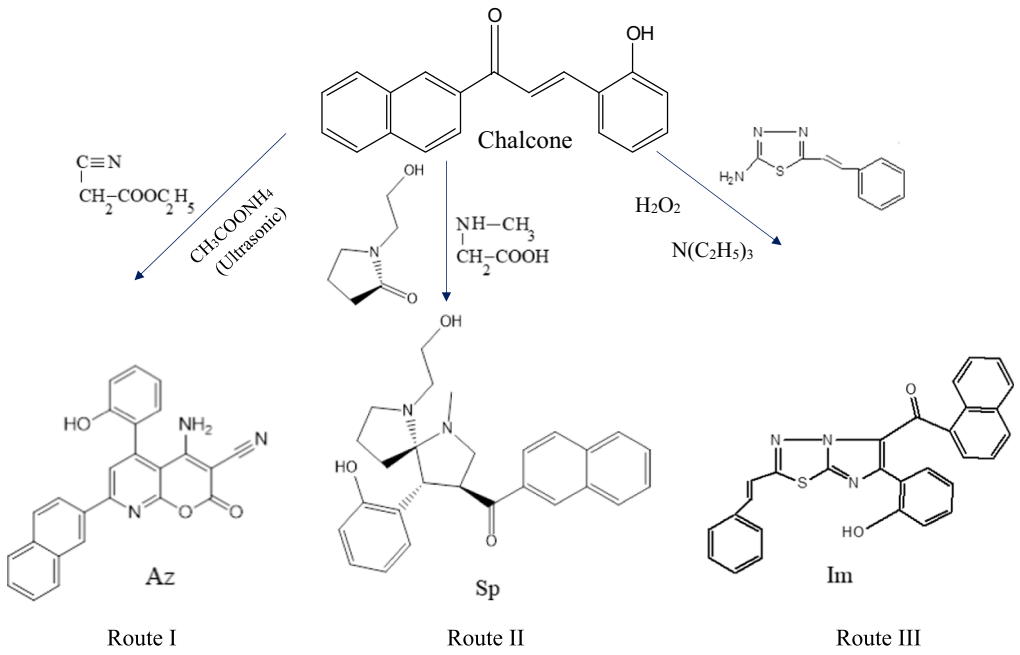

Fig. 1. Synthetic routes to azacoumarin (Az), spiro-pyrrolidine (Sp) and imidazothiadiazole (Im) heterocyclic compounds from chalcone derivative.

arylidene in form of *Z*-configuration), 7.38–7.86 (m, 11H, Ar—H) and 13.2 (br. s, 1H, acidic NH proton exchangeable by D_2O). ^{13}C NMR spectrum (Fig. S1, c) showed signals in ppm at: 40.0 (CH-CO), 125.5 (C_4 Ar), 132.3 ($C_{3,5}$ Ar), 134.8 (CH═), 137.4 (C_2 Ar), 138.4 (C_6 Ar), 142.5 (C═CH), 159.1 (CO azacoumarin). MS (*m*/*z*) 407/405. Elemental analysis for $C_{25}H_{15}N_3O_3$ (Az); calculated: % C, 74.07; % H, 3.73; % N, 10.36; found: % C, 73.89; % H, 3.68; % N, 10.21.

For the second procedure (*route II*), substituted spiropyrrolidine of IUPAC name (3*S*,4*R*,5*S*)-6-(2-hydroxyethyl)-4-(2-hydroxyphenyl)-1-methyl-1,6-diazaspiro[4.4]nonan-3-yl)(naphthalen-2-yl)methanone was prepared. Mixture of equimolar amount (0.05 mol) of chalcone, sarcosine and β-pyrollidone-ethanol were taken in about 10 ml of boiling aqueous methanol (1:3, *v*/v). The reaction mixture was refluxed for 6 h. The obtained precipitates were filtered off, washed several times by cold methanol and dried at 70 °C for 8 h, yielding D/L spiropyrrolidine derivative compounds. The chiral separation of the found D- and L-enantiomeric spiropyrrolidine derivative was proceeded on high-performance liquid chromatography (Agilent 1260 HPLC system, USA) with an auto-injector and optical rotatory detector, and column containing an efficient protein-based chiral stationary phase (human serum albumin immobilized to sulfhydryl reactive silica that had been activated by succinimidyl 4-(*N*-maleimidomethyl) cyclohexane-carboxylate). The chiral separation conditions were described in previous works [44,45]. Finally, the obtained spiropyrrolidine isomer was symbolized by "Sp".

Yield (76%); white solid; m.p. 188–190 °C. FTIR spectrum (Fig. S2, a) showed absorption band (in cm^{-1}) at: 3428, 3333 (OH), 3050 (CH aromatic), 1671, 1589 (C═O ketone). ^1H NMR spectrum (Fig. S2, b) represented signals (δ) in ppm at: 2.05 (s, 3H, CH_3CO), 2.46–2.71 (dd, 2H, CH_2 Aroyl), 3.21 (m, 1H, CH Aroyl), 3.24–3.28 (m, 1H, CHN), 3.57 (dd, 1H, J = 8.4 Hz, CHCOO), 3.68 (s, 2H, NCH_2Ph), 6.96 (d, 2H, J = 8.1 Hz, 2,6-CHAr), 7.02 (d, J = 8.1 Hz, 2H, 3,5-CHAr), 7.14 (dd, 3H, J = 8.4 Hz, 3,4,5-CH-ph), 7.20–7.28 (dd, 2H, J = 8.4 Hz, 2,6-CH-ph), 7.70 (s, 2H, 1,4-CH indole), 7.81 (d, 2H, 2,3-CH indole), 12.5 (s, 1H, NH-CO). ^{13}C NMR spectrum (Fig. S2, c) depicted signals (δ) in ppm at: 22.3 (CH_3), 43.1 (CH_2ph), 54.4 (C—C spiro), 60.1 (CHN), 122.0 (C_4 Ph), 124.1 ($C_{2,6}$ Ph), 127.3 ($C_{3,5}$ Ph), 132.1 ($C_{3,5}$ Ar), 136.3 ($C_{2,6}$ Ar) 190.1 (2CO Ar) and 199.3 (COO). MS (*m*/*z*) 432/430. Elemental analysis for $C_{27}H_{30}N_2O_3$ (Sp); calculated: % C, 75.32; % H, 7.02; % N, 6.51; found: % C, 75.14; % H, 6.79; % N, 6.36.

In the third procedure (*route III*), substituted imidazothiadiazole of IUPAC name (E)-(6-(2-hydroxyphenyl)-2-styrylimidazo[2,1-b][1,3,4] thiadiazol-5-yl)(naphthalen-2-yl)methanone was synthesized. Appropriate amount of substituted chalcone (2.35 g, 0.010 mol) and sodium hydroxide (0.96 g, 0.024 mol) were dissolved in acetone solution, acetone: methanol = 3:1 (*v*/v). The reaction mixture was treated with 30% *w*/*v* hydrogen peroxide (5 ml, 4.412 mmol), refluxed for 1 h, and left overnight at ambient temperature. The obtained solid fractions were filtered, washed several times by petroleum ether (b.p. 40°–60 °C), and then recrystallized from toluene. The purified solid product was fused in an oil bath in presence of TEA (0.25 ml, 1.80 mmol) for 5 min. The fused mixture was then gently poured into a solution of 2-amino-5-styryl-1,3,4-thiazole (1.89 g, 0.01 mol) dissolved in 50 ml of boiling aqueous ethanol (1: 3, *v*/v), and refluxed for 6 h. The formed precipitate was filtered off, washed several times by petroleum ether (b. p. 40°–60 °C), and recrystallized from dioxane to afford substituted imidazothiadiazole compound, being abbreviated by "Im".

Yield (60%); light yellow fine crystals, m.p. 176–178° C. FTIR spectrum (Fig. S3, a) demonstrated absorption band (in cm^{-1}) at: 3450, 3395 (OH), 3245 (w, NH), 3055 (CH aromatic), 1673, 1640 (CO), 1579 (C═N). ^1H NMR spectrum (Fig. S3, b) showed signals (δ) in ppm at: 2.54 (s, 3H, CH_3), 7.72 (s, 1H, dd, CH═, arylidine, 82% in form of *E*-configuration), 7.78 (s, 1H, CH═, arylidine, 18% in form of *Z*-configuration), 7.48–7.86 (m, 9ArH, aromatic protons) and 10.5 (s, 1H, s, acidic NH proton which exchanged in D_2O). ^{13}C NMR spectrum (Fig. S3, c) showed a strong and intense signal at 40.1 ppm (CH_3CO) linked with a series of weak signals (δ) in ppm at: 128.5 (C_4 Ar), 150.2 (C═CH), 156.0 (CNS), 162.2 (CN_2S), 165.1 (CO imidazole), 168.0 (CO amide), 190.2 (CO ketone). MS (*m*/*z*) 476/473. Elemental analysis for $C_{29}H_{19}N_3O_2S$ (Im); calculated: % C, 73.55; % H, 4.04; % N, 8.87; % S, 6.77; found: % C, 73.43; % H, 3.91; % N, 8.65; % S, 6.51.

2.4. Synthesis of magnetic Sinai organoclays

The iron-rich clay from Sinai was purified by being treated with 1 N HNO_3 (clay/H^+ mass ratio = 1/1) to swept up most of the foreign exchangeable cations in the clay sheets. This suspension was refluxed for 48 h, filtered, washed with distilled water several times to remove excess NO_3^{-1} ions and finally calcined at 270° C for 24 h in dynamic air.

The purified (acid-treated) clay was taken as reference material and nominated by ATT.

For the synthesis of modified Sinai clay by azacoumarin derivative compound (Az/ATT), appropriate amount of ATT (4.5 g) was suspended in DMF (40 ml) under vigorous stirring at room temperature for 24 h, keeping the clay concentration at 10% (wt/wt) to improve the dispersion of clay lamellae and facilitate drawing of heterocyclic compound by DMF molecules into clay interlayers [46]. A solution of 1.0 g of Az dissolved in 20 ml DMF was then gently poured into the clay suspension and stirred at room temperature for 48 h to ensure complete uptake of Az heterocyclic compound. The obtained precipitate (Az: clay = 18 wt%) was filtered, washed several times with distilled water and methanol, freeze-dried under vacuum, and then sieved to 200 μm mesh size. Synthesis of modified Sinai clay by substituting spiropyrrolidone (Sp/ATT) and imidazothiadiazole (Im/ATT) compounds were carried out following experimental conditions as above-described in preparation of Az/ATT.

2.5. Characterization techniques of magnetic Sinai organoclays

The molecular structure of the purified and the organoclays were studied through powder X-ray diffraction analysis adopting the XRD Philips PW3710-BASED diffractometer, operated with Ni- filtered CuKα radiation (λ = 1.5418 Å) at 40 kV and 40 Ma. The crystallite domain sizes of hematite particles in such clay samples were estimated from Debye-Scherrer equation [4]. Quantitative evaluation to the dispersion state of clay lamellae as a function of the used heterocyclic modifying agents was analyzed from the XRD spectra of the understudied organoclays by following Khederlou et al. approach [47], as being expressed from the given equations:

$$\overline{2\theta} = \frac{\sum_{i=m}^{n}(2\theta \ x \ I_i)}{\sum_{i=m}^{n} I_i} \tag{1}$$

$$\text{R.D.E.} = \left(1 - \frac{\bar{I}_{Test}}{\bar{I}_{Reference}}\right) \times 100 \tag{2}$$

where m and n exhibited the characteristic clays' peak interval as the peak intensity (I) became levelled off in both sides of the peak, $\overline{2\theta}$ was the mean diffraction angle of the basal d-spacing (001) peaks of the clays under investigated, R.D.E. was the relative degree of clay exfoliation, and finally $\bar{I}_{Test}$ as well $\bar{I}_{Reference}$ represented the mean diffraction intensities of the basal d-spacing (001) peaks of tested organoclays and reference ATT clay sample, respectively. Also, FTIR spectrophotometric was performed in a frequency range of 4000–400 nm, with 42 consecutive scans at a 2 cm^{-1} resolution using ATi Mattson, WI, 53717 model Genesis spectrometer (USA).

The potentials of the clays under study were measured by a Nano Series Zetasizer (MALVERN, United Kingdom). Each sample (0.5 mg/ml) was suspended in deionized water and adjusted at pH ~ 7.0 to meet the pH values of synthetic oils registered by Scott et al. [50]. The suspension was ultrasound-irradiated for 15 min, kept under vigorous stirring for 24 h at room temperature, and then the zeta-potential distribution curves were recorded at ambient temperature. Also, the particle size distribution (hydrodynamic diameter) of the modified clay samples was also evaluated by dynamic light scattering (DLS) using the previously described Zetasizer Nano Series instrument, following the aforesaid procedure.

The morphology of the understudied clay samples and the size of their correspondingly existed hematite particles were examined by high-resolution transmission electron microscope (HRTEM, JEOL-2100) operating at 200 KV with resolution of 0.14 nm.

The textural characteristics of these clays were assessed by the aid of N_2 adsorption-desorption isotherms measured at −196 °C, for surface area determination and pore size analysis [48,49]. A NOVA 3200 apparatus (USA) was used, where the samples were out gassed at 150 °C for 4 h at 10^{-5} Torr. Also, the magnetic properties of the understudied clay samples were measured at room temperature using a vibrating sample magnetometer (740 0-1 VSM, U.S., Lake Shore Co., Ltd., USA) in a maximum applied field of 20 kOe. From the obtained hysteresis loops, the coercivity (H_{ci}), remanent magnetization (M_r) and squareness (M_r/M_s) were determined.

2.6. Sustainable approaches in lubricant oil industry using magnetic organoclays

2.6.1. A strategy for stimulating electrical, physicochemical and lubricant properties of base oil

To evaluate the electrical property of the base oil (given by co-operation petroleum Co., Egypt), 50 ml of this oil was dissolved in 200 ml xylene and added to 250 ml of a mixture of methanol/n-butanol (1:2) applying the standard method in ASTM [51]. Each magnetic organoclay sample was suspended in 100 ml of the as-prepared mixed solution by a concentration of 500 mg/l. The suspension was then ultrasound-irradiated till forming uniform dispersion. Apart from the conventional use of salinometer (SCO 1, Anton paar GmbH, AU) in measuring chloride concentration in crude oil [51], further explored area to the application of salinometer, in this study, was drawn based on realizing the relationship between current (I, mA) and voltage (V, mV) for the obtained suspensions and investigating the electrical stimulation efficiency (ESE, %) of each organoclay as expressed by Eq. (3).

$$\text{Electrical stimulation efficiency } (\%) = ((S_T - S_o)/S_T) \times 100 \tag{3}$$

where, S_T and S_o were assigned to the slopes of the linear I-V characteristic of the tested suspensions and the base-oil solution free from clay fine particles, respectively.

Physicochemical properties, such as flash and pour points, and total acid number, of the base oil and the various base-oil suspensions of 500 mg/l concentration of the understudied organoclays were carried out applying ASTM methods [52,53]. Furthermore, the lubricating behavior in terms of friction coefficient and wear scar diameter (WSD) was investigated for both the base oil and the found base-oil suspension exhibiting the highly relevant physicochemical characteristics to those of the base oil. The commercial engine oil (MISR PHOENIX, 5 W/40, Misr petroleum Co., Egypt) was used as reference lubricant oil for a comparative study. Such lubrication characteristics were evaluated by a four-ball test machine (Ducom Instruments Pvt. Ltd., India), where a 12.7 mm steel ball under the load of 392 N is rotated against three stationary steel balls for 60 min with a speed of 1200 rpm at 75° C, as per the ASTM D4172 standard test method.

2.6.2. Strategic management processes for regeneration of waste lubricant oil

The waste lubricant oil was obtained and collected from EPRI (Egyptian petroleum institute) oil service station. At first, the waste oil was purified through being centrifuged at 1500 rpm for 30 min and left to settle for 2 h, and then filtered by Buchner funnel using a vacuum pump [54]. Secondly, the purified oil was mixed with extracting solvent mixture (xylene: n-butanol: methanol 1:1:1 (v/v)) at oil to solvent ratio of 1:3 by volume (v/v) following procedure discussed elsewhere [54,55]. The mixture was refluxed at 70° C for 2 h under vigorous stirring and stored for several days for sedimentation of suspended particles by gravity. Afterwards, the mixture was distilled at 130 °C and raffinate oil was collected [55]. Along with sedimentation, filtration, solvent extraction and distillation, treating of raffinate oil with various organo-modified clay samples at proportion of 1:5 (w/w) was the pivotal and the final step in the management of regenerated oil. The raffinate oil was passed through opened glass column (15 cm × 1 cm i.d.) packed with 200-mesh organoclay powder at oil/organoclay weight ratio of 1: 15. Elution was carried out by cyclohexane. The

elute was freed of solvent (cyclohexane) by distillation. The obtained separated oil (regenerated oil) was then dried in vacuum oven till constant weight was determined [55].

Physicochemical characteristics in terms of density, Kinematic viscosity, viscosity index, pour and flash points, and total acid number (TAN), for the waste lubricant oil (after purification) and the various regenerated oils were evaluated according to the standard methods in ASTM [52,53]. The color evaluation of these oils was conducted using UV–Visible spectroscopy (Model UV-1700, Shimadzu, Kyoto, Japan) by scanning the regenerated oils at the visible region. Also, the physicochemical characteristics of the waste oil and the 5 W/40 engine oil (reference oil) were used for comparative study.

2.6.3. Production strategy of acetic acid from waste lubricant oil

The waste lubricant oil was purified and subjected to solvent extraction process adopting the above-mentioned procedure in Section 2.6.2. to produce raffinate oil. For each experiment, 25 ml of this raffinate oil was vigorously stirred with the examined organoclay catalyst sample of 500 mg/l concentration in a 50 ml two-necked flask. The suspension was refluxed at 150° C under O_2 bubbling at flow rate 1 ml/min for 72 h. The fluidized product (oxidized oil) was filtered to remove the remained organoclay particles, and then analyzed by a gas chromatograph-flame ionization detector (GC-FID, 7890A, Agilent Instruments) using stainless steel HP-5MS column (30 m × 250 μm × 0.25 mm) and helium (99.999% purity) as a carrier gas. The column temperature was initially kept at 35 °C for 10 min, then heated to 150 °C at a rate of 2 °C/min and finally heated at 280° C for 10 min with a rate of 20 °C/min, holding the FID temperature at 280 °C [37]. Acetic acid (Ac), as the desired detectable product of catalytic oxidation of raffinate oil, could be calculated using Eq. (4).

$$\text{Yield of Ac (wt\%)} = (M_{EA}/M_{oil}) \times 100 \quad (4)$$

where, M_{EA} and M_{oil} were the mass of the produced acetic acid by catalytic oxidation of raffinate oil using various tested organoclays and the mass of initial feed of raffinate oil, respectively, estimated from the corresponding chromatographies peak areas.

3. Results and discussions

3.1. DFT studies of O, N, S heterocyclic compounds under investigation

Density functional theory model carried out for Az, Sp and Im heterocyclic compounds can give insights into their optimized (most stable) structures and their corresponding electron clouds, as shown in Fig. 2. The regions of the highest electron density (HOMOs) are more susceptible to electrophilic attack, while the LUMO regions (anti-bonding orbitals) are highly subjectable to nucleophilic attack. As can be seen in Fig. 2, the electron density is continuously saturated all over the Az and Im molecules indicating presence of limitless electron delocalization onto planar compounds. Meanwhile, the electron cloud for Sp compound is discontinuously distributed across the whole molecule demonstrating non-planarity in the geometry of Sp molecule (Fig. 2). In case of Az and Im heterocyclic compounds, the HOMOs are distributed over azacoumarin and fused imidazothiadiazole rings, respectively, and the LUMOs are almost concentrated on naphthalene rings. These findings infer that azacoumarin and imidazothiadiazoles units are the most active centres for electron transfer in Az and Im reactions,

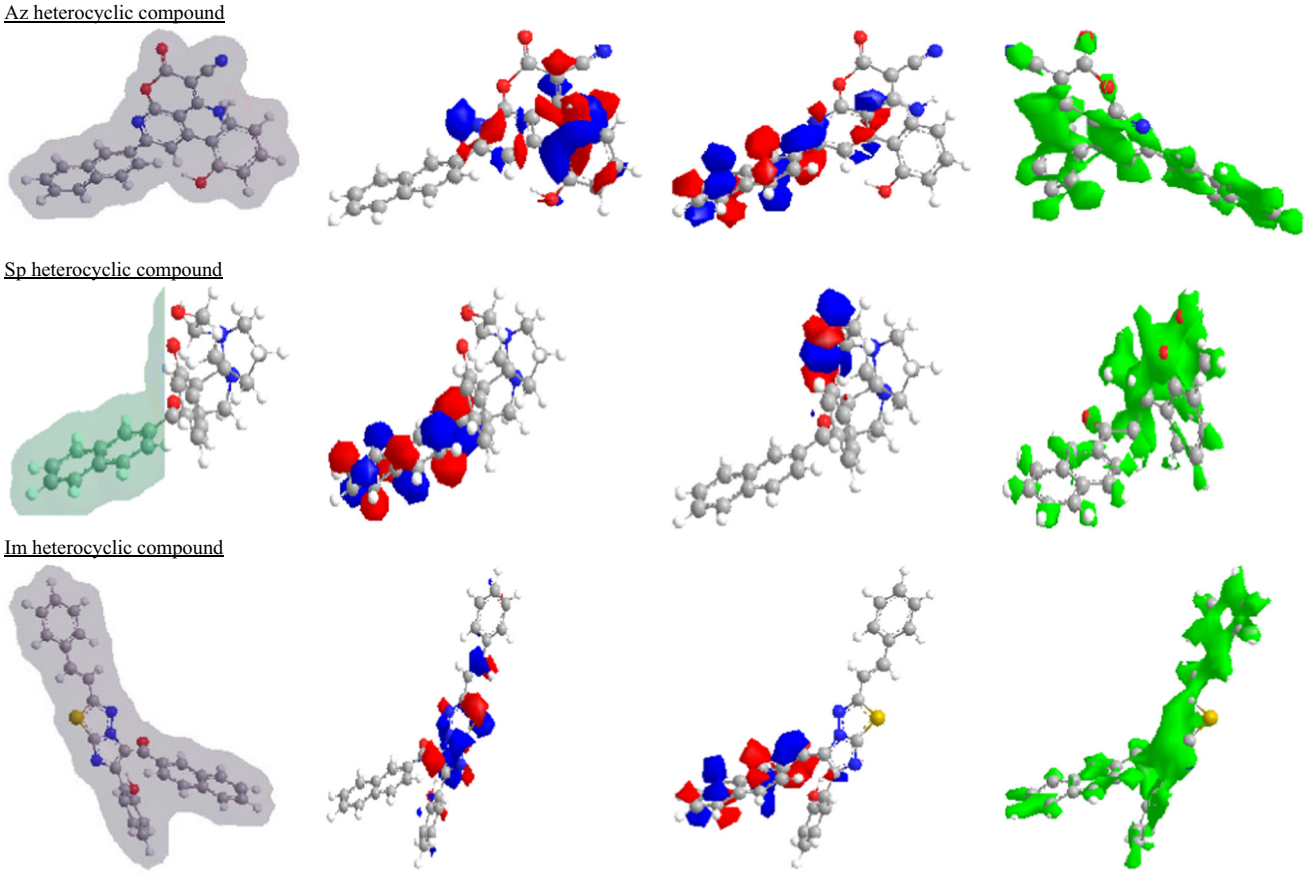

Fig. 2. Overall electron density of the optimized structures (left), highest occupied molecular orbitals (left in middle), lowest unoccupied molecular orbitals (right in middle), and solvation affinity (right) for the various as-synthesized O, N, S heterocyclic compounds. Color index: White balls = H, Grey balls = C, Blue balls = N, Red balls = O, yellow balls = S, blue patches = electron-rich figures, red patches = electron-deficient figures, and Green patches = DMF solvent. (For interpretation of the references to color in this figure legend, the reader is referred to the web version of this article.)

respectively. In contrast, the HOMOs of Sp compound are sieged beyond the naphthalene ring, leaving the LUMOs to be distributed over the remained extended structure of the substituted pyrrolidine rings, thus reflects the influence of non-planarity on controlling the Sp reactions (Fig. 2). It can be also noted that the plane of symmetry in Az and Im heterocyclic compounds increases from their solvation (hydration) behaviour, whereas the asymmetrical geometry of Sp compound reduces its solvation affinity, cf. Fig. 2. The parameters derived from DFT study for various as-synthesized heterocyclic compounds are represented in Table. 1. It is worthy to consider Az compound as a highly nucleophilic molecule enriched by polar and solvated sites resulting from its elevated ω, μ and E_H values, see Table. 1. Unlikely, Sp compound records the lowest σ, μ and E_H values confirming the dominant contribution of electrophilic centres in the various interacting modes of Sp. The DFT parameters of Im compound seems to be averaged with those belonged to Az and Sp compounds, demonstrating the capability of Im molecule to behave either like nucleophile or electrophile.

For giving more clarity to the electronic nature of the compounds under study, the energies corresponding to their HOMOs and LUMOs are obtained and listed in Table. 1. As the gap energy value (ΔE), where $\Delta E = E_{LUMO} - E_{HOMO}$ [42,43], assesses the reacting affinity of any organic compounds [45], the ΔE values for the as-synthesized compounds are also listed in Table. 1. The Az compound exhibits the highest ΔE value demonstrating hard contribution of LUMOs in the reactions of Az molecule with exclusive share to HOMO electrons (via a donation progress) in Az interactions. Meanwhile, the Sp compound, as a "soft" molecule [56], possesses the lowest gap-energy value inferring that the reactions of Sp compound take place majorly by unlimited hosting of electrons in its vacant orbitals (LUMOs) adopting a withdrawn progress. These facts are in concurrence with the above-described nucleophile and electrophile nature of Az and Sp compounds, respectively, by other DFT parameters (σ, μ and E_H). The Im compound, thereby its median ΔE value, is predicted to be efficiently reactive molecule that apt to donate electrons from HOMOs as well as host accepted electrons by LUMOs.

3.2. Physicochemical features of iron-rich Sinai clay modified by O, N, S heterocyclic moieties

3.2.1. Structural investigation

The XRD patterns of clay reference material (ATT) and the various iron-rich organoclay samples are shown in Fig. 3(a). For ATT sample, the characteristic (001) reflection of montmorillonite at ~13.15° 2θ of d-spacing 7.18 Å is appeared, as represented by the 1st enlarged view in Fig. 3(a), linked to presence of sharp and intense reflections of quartz and illite at 26.78° 2θ and 27.47° 2θ, respectively [57]. The reflections around 19.86° 2θ are ascribed to the summation of hk indices of (02) and (11), which arise from the natural random stacking in the clay sheet structure [4]. Poor reflected radiations at 2θ = 33.72° and 37.26° appear belonging most probably to (104) and (110) lattice planes of crystalline hematite (α-Fe_2O_3) particles, respectively [58], thus indicates veiling of hematite particles within clay interlayered spaces. To exclude leaching of iron ions from naturally iron-rich Sinai clay by acid treatment, the total composition of the dry basis of ATT sample was measured affording hematite content matched closely to that of the natural clay sample, where SiO_2 (58.45 wt%); Al_2O_3 (19.16 wt%); Fe_2O_3 (10.24 wt%); Na_2O (0.45 wt%); CaO (0.27 wt%); MgO (0.51 wt%); K_2O (0.18 wt%); TiO_2 (0.37 wt%).

By modifying the reference ATT sample with azacoumarin derivative compound, the basal (001) peak is shifted to lower 2θ (viz., 11.21°) and the interlamellar spacing is significantly expanded from 7.18 Å in ATT to 15.93 Å in Az/ATT, cf. 2nd enlarged view in Fig. 3 (a), while the reflection of α-Fe_2O_3 particles are intact. Such results affirm typical intercalation of azacoumarin substituent in the ATT clay sheets without disturbing the concealed behavior of hematite species. For Sp/ATT clay sample, a broad (001) band of very low intensity (0.72%) at 2θ ~ 12.57° arises (3rd enlarged view in Fig. 3, a) linked with marked intensification to the quartz and k ≠ 3n reflections [(02) and (11)]. These results point to marked deterioration in the crystallinity and the interlamellar structure of clay forming typical clay exfoliated system. Such exfoliating profile seems to dawn hematite particles showing strongly their whole characteristic reflections at 2θ = 33.72°, 37.26°, 50.72° and 60.05° referring to (104), (110), (024) and (214) lattice planes, respectively [58]. The average size of hematite particles is found to be close to 20 nm, as calculated from Debye-Scherrer equation [59], based on the FWHM of the peak corresponding to (104) plane. In case of Im/ATT sample, the (001) reflection of ATT is further shifted to lower 2θ (~10.03°) with d spacing of 25.8 Å, as seen from the 4th enlarged view in Fig. 3a, revealing presence of pronounced intercalated clay system by imidazothiadiazole derivative compound. Such considerable widening in the clay interlamellar spacing allowed hematite particles to be unveiled, showing their entire lattice fringes (Fig. 3a). The average size of hematite particles in Im/ATT sample is nearly half that it is in Sp/ATT sample. These results may possibly buttress presence of clay exfoliation to some extent. The XRD patterns of the various organoclays demonstrate presence of quartz, illite and two-dimensional (hk) reflections at their original position in ATT clay sample. For more confirmation, Khederlou et al. mathematical model for XRD interpretation in clay exfoliated system is applied [47], conducting a remarkable increase in the degree of exfoliation from 35% in the case of Im/ATT to 88% in Sp/ATT clay system.

The FTIR spectra of reference ATT and various organoclays are depicted in Fig. 3 (b). The FTIR spectrum of ATT shows two strong absorption bands in 990–1270 cm^{-1} and 3150–3660 cm^{-1} regions, reflecting the stretching vibrations of Si—O groups in the layered silicate structure (apical oxygens of SiO_2 tetrahedra) and O—H groups in the inner surfaces of clay sheets, respectively [4,57]. The FTIR bands at 915, 690, 564 and 468 cm^{-1} belong to AlAlOH, Si—O—Si $_{out\text{-}of\text{-}plane}$, Si-O-Al (Al is an octahedral cation), and Si—O—Si $_{in\text{-}plane}$ bending vibrations, respectively [57]. Also, the band at 790 cm^{-1} corresponds to the disordered OCT (opal-CT as para crystalline silica, $SiO_2 \cdot H_2O$) [4]. Upon modification of ATT sample by azacoumarin substituent, most of the characteristic bands of this clay, except the OCT band that remains intact, are blue shifted indicating successful intercalation of such heterocyclic compound into the layered clay material. Such intercalated clay system seemingly weakens the interaction between neighbored clay sheets, allowing each one to behave individually.

On the contrary, the characteristic absorption bands of Sp/ATT clay sample are red shifted accommodating existence of an intimate interaction between the spiropyrrolidine derivative compound and the lattice structure of clay, which encompasses surface hydroxyls, and basal bridging and apical oxygens in the tetrahedral SiO_2. Comparing with the FTIR spectrum of ATT reference sample, the stretching vibrations

Table 1
DFT parameters calculated for O, N, S heterocyclic compounds under study.

Heterocyclic compounds	Electron density[a], $\sigma \times 10^3$ (eV/nm^2)	Dipole moment, μ (Debye)	Hydration, E_H (k cal mol^{-1})	E_{HOMO} (eV)	E_{LUMO} (eV)	ΔE (eV)
Az	6.17	13.64	−16.23	−9.81	−5.02	4.79
Sp	3.48	0.40	−19.23	−3.88	−3.13	0.75
Im	4.67	1.92	−18.25	−9.17	−5.20	3.97

[a] Estimated from dividing nucleophilicity index (ω, eV) of the various heterocyclic compounds under study by their corresponding DFT surface area (A, nm^2).

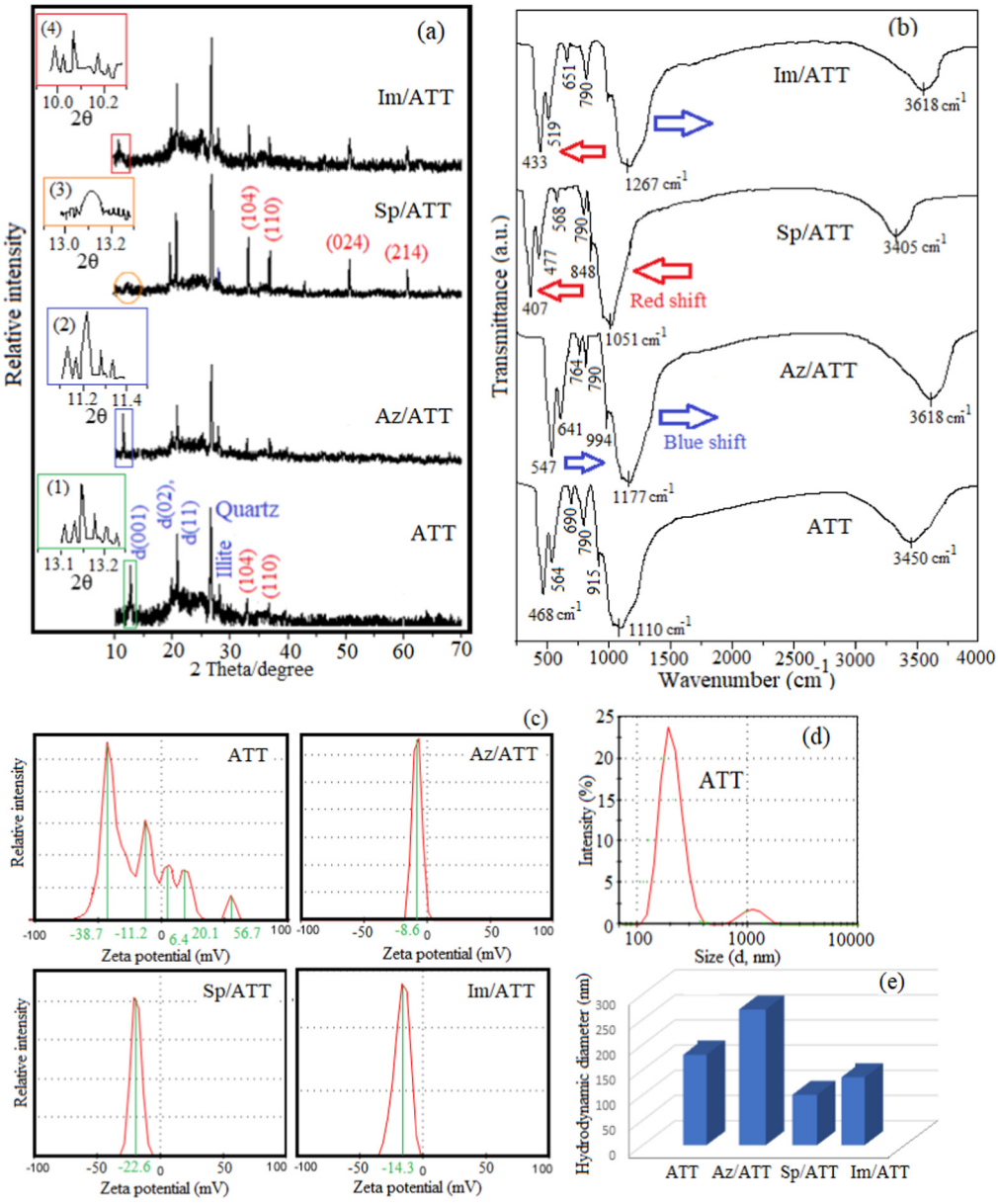

Fig. 3. XRD patterns (a), FTIR spectra (b), zeta potential distribution curves (c), hydrodynamic particle size distribution (d) and average hydrodynamic particle sizes (d) of clay samples under study.

of the apical oxygens in the silicate layered structure of clay are red shifted from 990 to 1270 cm^{-1} region to 850–1210 cm^{-1} region, the bending vibrations of the Si—O—Si basal bridging oxygens are shifted to lower frequencies from 468 cm^{-1} to 407 cm^{-1} and from 690 cm^{-1} to 568 cm^{-1}, and the O—H groups is downshifted from 3150 to 3660 cm^{-1} region to 3110–3500 cm^{-1} region, see Fig. 3, b. Such a firm correlation between clay sheets and Sp molecules may be indicative of the presence of an exfoliated clay system.

For Im/ATT sample, the imidazothiadiazole derivative compound tends most probable to interact tightly with the basal bridging oxygens resulting in marked red-shifting to Si-O-Si and Si-O-Al bending vibrations, when compared with reference ATT sample, from 468 cm^{-1} to 433 cm^{-1} and from 564 cm^{-1} to 519 cm^{-1}, respectively (Fig. 3, b). In a different attitude, Im molecules prone also to weaken the interaction between clay sheets from the sides enriched by surface hydroxyls and apical oxygens of SiO_2 tetrahedra developing remarkable shifting of their peaks to higher frequencies, compared to those recognized in reference ATT sample, from 3150 to 3660 cm^{-1} region to 3250–3720 cm^{-1} region and from 990 to 1270 cm^{-1} region to 1060–1350 cm^{-1} region, respectively (Fig. 3, b). These findings strongly suggest the capability of this heterocyclic compound to suit the exfoliated as well the intercalated layers' profiles in one-unit clay system.

3.2.2. Surface charges and hydrodynamic particle size distribution

The obtained surface charges, governed by zeta potential distribution curves, average zeta potentials (ζ_{av}) as well as hydrodynamic particle size measurements of reference ATT and various organoclays under study are illustrated in Fig. 3(c, d and e). As clearly shown from the zeta potential distribution curve of ATT, large populations of clay particles of diverse ζ_{av} values (from −38.7 mV to +56.7 mV, in penta-modal size distribution) seem to exist confirming a significant haphazardness in the aggregation behaviour of clay particles. This phenomenon is also evidenced by the recorded wide range of hydrodynamic particle size distribution of ATT clay sample that covers proportions from 100 nm to 3000 nm, cf. Fig. 3, c and d. Modifying the ATT clay sample by the various understudied heterocyclic organic compounds develops sharp intense unimodal charged systems at different ζ_{av} values, further indicates the affinity of these organic compounds to alter and reorganize the

aggregation properties of clay. The negative charges of the ζ_{av} values increased (from −8.6 mV to −14.3 mV to −22.6 mV), according to the organo-modifier used, in the order: Az/ATT < Im/ATT < Sp/ATT, cf. Fig. 3, c. These results are much more confirmed by the measurement of the average hydrodynamic particle sizes of the various organoclays under study that decreased from 270 nm to 135 nm to 100 nm, according to the organo-modifier used, in the order: Az/ATT > Im/ATT > Sp/ATT (Fig. 3, e). It is discernible from these findings that each organo-modifier seems to go along reorganization of the surface charges of ATT through adopting different ways. For Az/ATT, the azacoumarin derivative compound tends probably to merge clay layers forming large agglomerates of semi-neutralizing character. In case of Im/ATT and Sp/ATT samples, the imidazothiadiazole as well spiropyrrolidine substituents most probable shuffle the ordered feature of clay sheets, conducting higher negatively charged particles of lower sizes rather than those obtained by modifying ATT with Az molecules, i.e. the disordering affinity of Sp molecules toward clay sheet structure is greater than that of Im molecules.

3.2.3. Morphology and textural investigations

The morphology of various organoclays is examined via TEM as illustrated in Fig. 4. The ATT sample, in micrograph (a), shows a compacted, linear and regular clay sheet structure with highly ordered stacking mode. By modifying this sample with Az heterocyclic compound (Fig. 4b, i), the clay layer stacking is markedly interrupted accompanied by widening of the interlayer spaces, thus allows free-sliding of clay

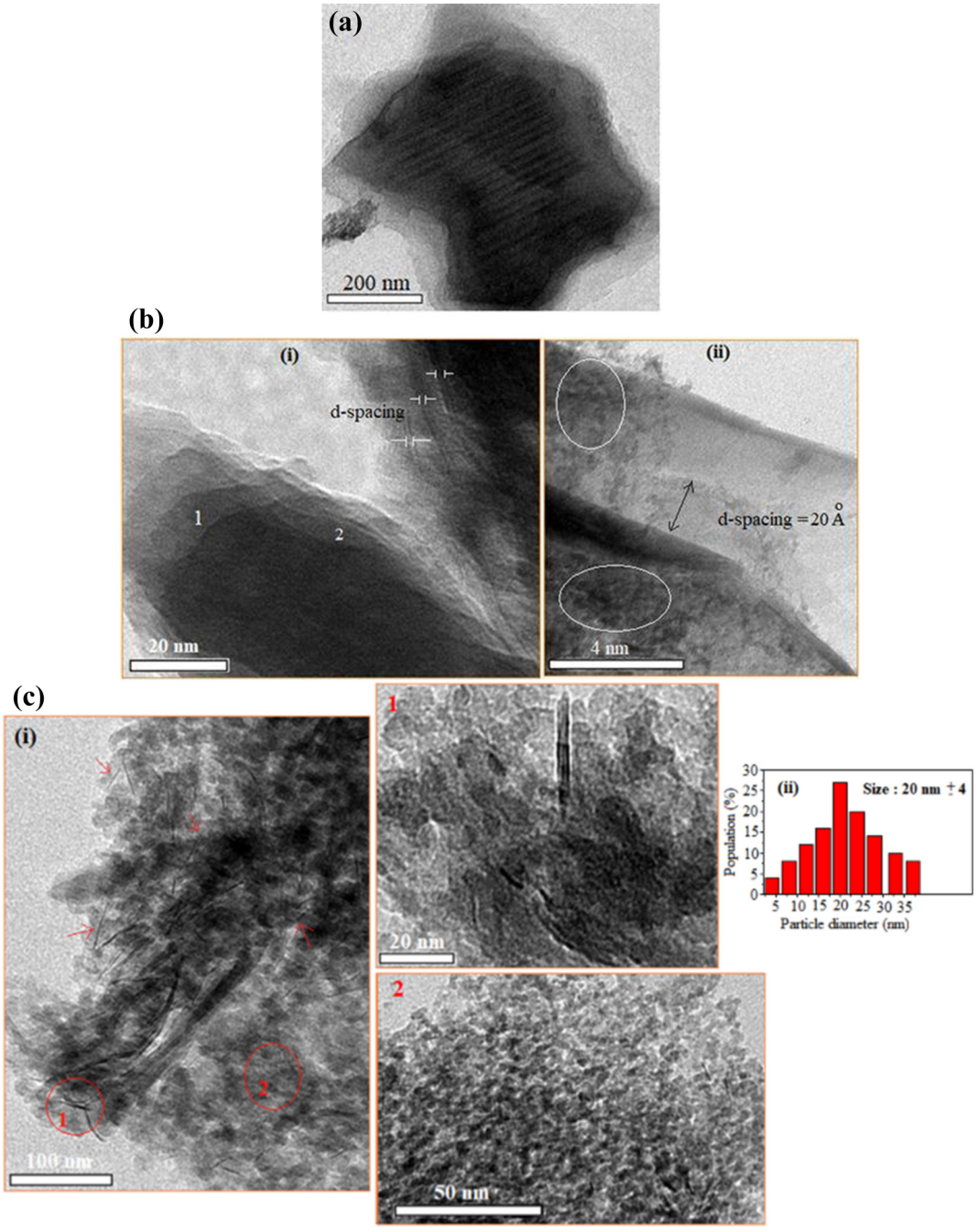

Fig. 4. HR-TEM micrographs of: (a) ATT, (b) Az/ATT, (c) Sp/ATT and (d) Im/ATT. The inset images (1 and 2) in micrographs (c) and (d) represent the enlarged views for the organoclay under study. Pictures (ii) of Sp/ATT and Im/ATT samples represent the particle size distribution of the contained hematite species.

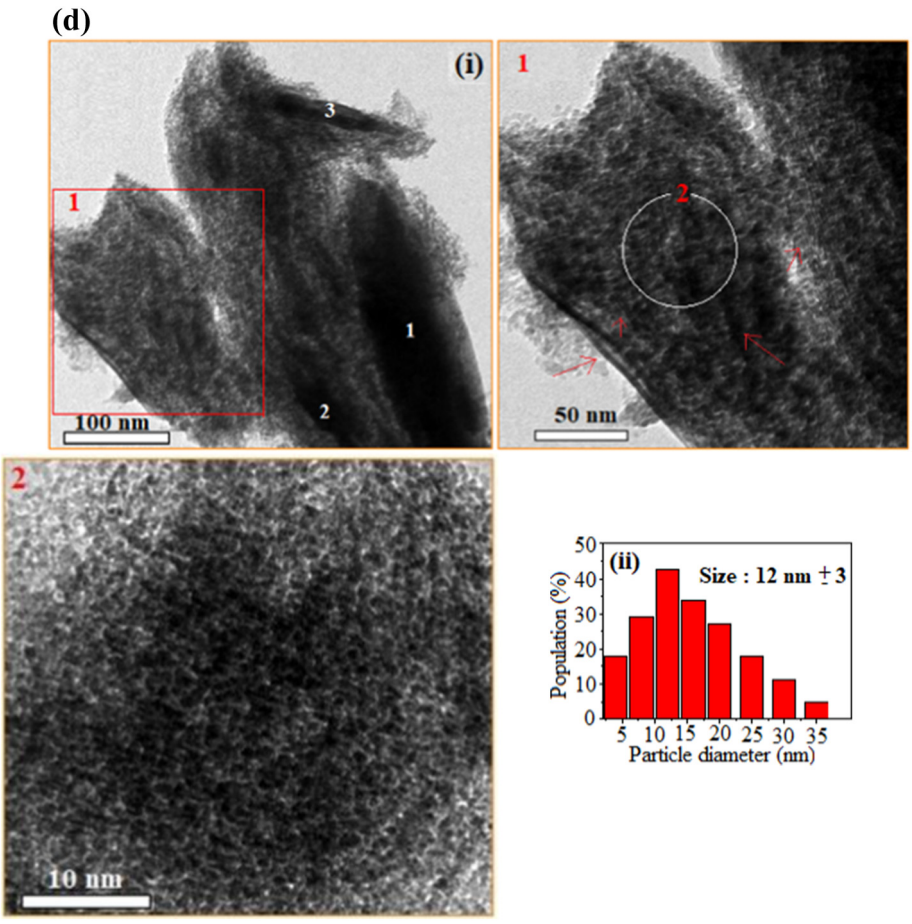

Fig. 4 (*continued*).

sheets over each other (cf. elements 1 and 2 in Fig. 4b, i). The interlayer spacing is further distinguished at higher magnification showing lodgement of angstrom-size hematite particles (as represented by white circles) within the interlayer space of ~20 Å intercalation distance, Fig. 4b, ii. These findings probably reveal the efficient insertion of Az molecules inside the clay layers, keeping all layers in-parallel with building up a fully intercalated clay system. For Sp/ATT sample, the TEM image (Fig. 4c, i) affirms the applicability of Sp compound to enter and go further in clay galleries peeling the clay platelets apart (as represented by red arrows), thus causes a dramatic loss in the ordered layer structure of clay and improves full clay exfoliation. The clay platelets appear as nano-fibrils of ca 4 nm diameter and an average length of 20 nm, as being represented from the HR-TEM magnified image of the 1st red circle in Fig. 4c, i. Such clay exfoliating character is coherent with the existing literature in suggesting the peeling mechanism as a function of compounding resins like nylon 6 and 12 with the clay layered structure via using various extrusion conditions [60,61]. As can be seen from the magnified content of the 2nd red circle in Fig. 4c, i, clay exfoliation with respect to the used Sp modifier seems to encourage dispersal floating of hematite nanoparticles over the exfoliated clay platelets adopting average particle size close to 20 nm, as estimated from the size distribution histogram in Fig. 4c, ii. This pronounced exfoliating efficiency possibly refers to the strong interaction between Sp compound and the various accommodated sites in clay layer structure (e.g. hydroxyls, basal and apical bridging oxygens), as demonstrated by FTIR analysis. In case of Im/ATT, the compatibility between imidazothiadiazole substituent and clay sheets inspires shearing of clay layers, creating a partially intercalated/exfoliated system in which the intercalated stacks are much more separated (as represented by elements 1–3 in Fig. 4d, i) associated with presence of few exfoliated nanometric flakes, cf. red arrows in the enlarged image (1) of Fig. 4d, i. In image (2) of Fig. 4d, the HR-TEM image magnifies the contents in the white circle (in image (1) of Fig. 4d) indicating presence of well-dispersed spheroidal hematite nanoparticles beyond exfoliated flakes with ~12 nm in diameter, as estimated from the size distribution histogram in Fig. 4d, ii. Such panoramic view for clay matrix is congruent with previous work [62]. All the above-mentioned findings are kind consistent with the reporting XRD data.

The textural characteristics of reference ATT and various organoclay samples are recognized using N_2 adsorption-desorption isotherms (Fig. 5a). It is discernable that all the isotherms are of type II per IUPAC classification in P/Po region ~0.20–0.99, exhibiting closed hysteresis loops at relative pressure close to 0.6. All the hysteresis loops belong mainly to H3 type developing mesoporous materials that have fewer micro-sized pore dimensions, often associated with aggregated plate-like particles of slit-shaped pores, [48,49]. The different surface parameters derived from adsorption-desorption isotherms are summarized in Table 2. The specific surface areas (S_{BET}, $m^2\ g^{-1}$) are derived from the linear relation of BET plots [48]. The total pore volumes (V_p, ml g^{-1}) are estimated from the amount of N_2 adsorbed at 0.99 P/P_o [57]. The average pore radii (r_p, Å) are calculated according to Eq. (5), assuming the slit-shaped pore model [49,57].

$$r_p(\text{Å}) = (2V_p/S_{BET}) \times 10^4 \quad (5)$$

The most abundant hydraulic pore radii ($r_{h\ most.abund}$, Å) are demonstrated from pore size distribution (PSD) curves (Fig. 5b) using Barrett-Joyner-Halenda method (BJH), assuming parallel plate pore model from the desorption branch of the obtained isotherms [48,49,57].

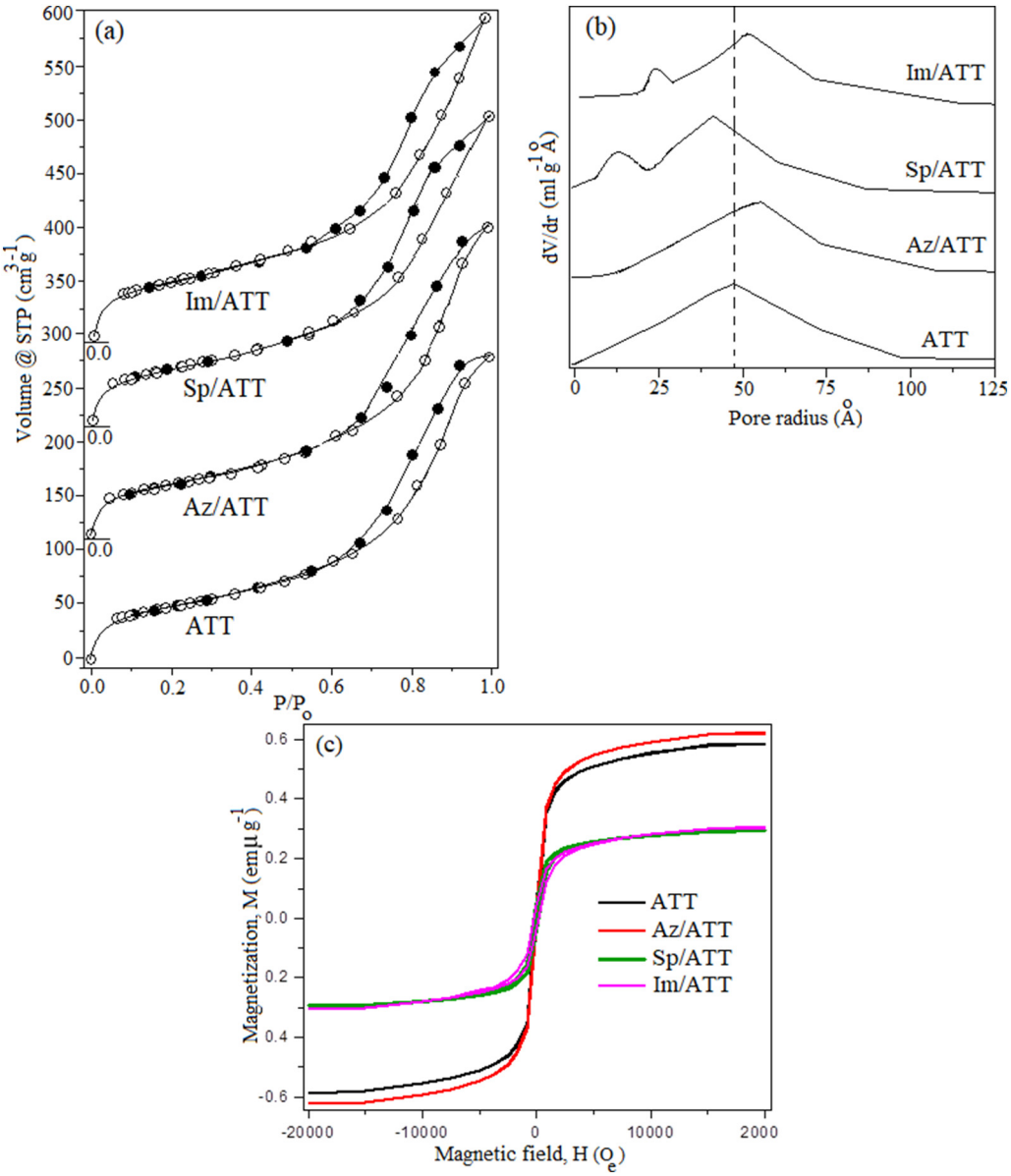

Fig. 5. (a) Adsorption-desorption isotherms of N_2 at −196 °C, (b) pore size distribution curves and (c) magnetic hysteresis loops at room temperature for the various clay samples under study.

As can be seen from Table 2, for Az/ATT clay sample, the specific surface area and the total pore volume of reference ATT sample are significantly reduced (viz. from 170 $m^2\ g^{-1}$ to 151 $m^2\ g^{-1}$ and from 0.421 ml g^{-1} to 0.379 ml g^{-1}, respectively) associated with remarkable increment of the pore dimensions, namely, r_p (from 49 Å to 53 Å) and $r_{h\ most.abund}$ (from 47 Å to 57 Å, in a unimodal PSD covering wide range of 12–100 Å, Fig. 5b). Such results presumably attributed to the efficient intercalation of ATT clay layers by the azacoumarin derivative compound. On contrary, modifying the reference ATT clay sheets with spiropyrrolidine derivative compound shows elevation in S_{BET} (from

Table 2
Textural characteristics and magnetic properties of clay samples under investigation.

Samples	Textural characteristics					Magnetic properties		
	S_{BET}[a] ($m^2\ g^{-1}$)	V_p[b] (ml g^{-1})	r_p[b] (Å)	$r_{h\ most.abund}$[c] (Å)	V_{micro}[d] ($cm^3\ g^{-1}$)	H_{ci} (O_e)	M_r (emμ g^{-1})	Squareness (M_r/M_s)
ATT	170	0.421	49	47	0.212	79	0.037	0.063
Az/ATT	151	0.379	53	57	0.107	71	0.033	0.058
Sp/ATT	180	0.476	45	10, 42	0.327	208	0.040	0.131
Im/ATT	160	0.405	52	18, 52	0.164	171	0.040	0.138

[a] Calculated from N_2 adsorption-desorption isotherms using the BET equation.
[b] Determined from N_2 adsorption-desorption isotherms.
[c] Determined from pore size distribution curves (PSD).
[d] Determined from t-plot method for micropore analysis.

170 to 180 $m^2 g^{-1}$) and V_p (from 0.0421 to 0.476 ml g^{-1}), and depression in r_p (from 49 Å to 45 Å) linked with uneven bimodal PSD, where large fractions of pores of $r_{h\ most.abund} = 10$ Å and 42 Å can be noticed, Fig. 5b. These findings clearly suggest the affinity of Sp molecules to sturdily deform (and/or exfoliate) the lamellar structure of ATT and change its mesoporous nature to form a microporous high-surface area clay system. Upon modification of ATT sample by imidazothiadiazole derivative compound, a decrease is noticed in S_{BET} (from 170 to 160 $m^2 g^{-1}$) and V_p (from 0.0421 to 0.405 ml g^{-1}), accompanied with an increase in r_p (from 49 Å to 52 Å) and $r_{h\ most.abund}$ (from 47 Å to large populations of mesopores ~ 52 Å, Table 2) confirming entrapment of Im molecules inside ATT clay interlayers, suggesting presence of an intercalated system. Interestingly, the pore size distribution of Im/ATT sample (Fig. 5b) serves a bimodal system that contains noticeable fractions of micropores having hydraulic radius of ~18 Å. This finding most likely clarifies the slight tendency of Im molecules to alter the surface properties of clay layers and disorganize (or exfoliate) their interlamellar structure.

For more confirmation to the above-mentioned porous structural studies, the "t-plot method" for micropore analysis that was developed by De Boer et al. [48] has been used for estimating the actual micro pore volume (V_{micro}, $cm^3 g^{-1}$) of the obtained organoclay samples and introduced in Table 2. It is clearly obvious that the order of micropore volumes for organoclays is congruent with that of surface areas, whereas the Sp/ATT records the highest surface area (180 $m^2 g^{-1}$) and micropore volume (0.327 $cm^3 g^{-1}$), and the Az/ATT possesses the lowest values (of $S_{BET} = 151$ $m^2 g^{-1}$ and $V_{micro} = 0.107$ $cm^3 g^{-1}$). It is conceivable to hypothesize that the pore structure in Sp/ATT is mainly confined to micropores, meanwhile the porosity in Az/ATT exhibits poor contribution to micropores at the expense of the mesoporous nature of this organoclay that owes hydraulic pore radius ~57 Å. In case of Im/ATT sample, considerable fractions of microporosity ($V_{micro} = 0.164$ $cm^3 g^{-1}$) seem to be concomitant with the predominant mesoporous structure (Fig. 5b).

3.2.4. Magnetic investigations

The magnetization curves (M–H plots) obtained through the magnetic measurements of reference ATT sample and various organoclays (Az/ATT, Sp/ATT and Im/ATT) made at room temperature are shown in Fig. 5c. It is clear from the graph that the magnetic properties of ATT clay sample are highly affected by the type of organo-modifiers, whereas magnetisation loops of Sp/ATT and Im/ATT are saturated at lower magnetic field rather than that seen by Az/ATT. The observed magnetic parameters, viz. coercivity (H_c), remanent magnetization (M_r) and squareness (M_r/M_s) are given in Table 2. The values of coercivity and remanent magnetization of Az/ATT are close to those of reference ATT sample with percentage deviation around ±10% (71 Oe and 79 Oe for coercivity, and 0.037 emμ g^{-1} and 0.033 emμ g^{-1} for remanent magnetization, respectively) suggesting that the overall lamellar structure of clay remains almost intact in presence of Az modifier. As such, the conceivable hosting of clay interlamellar spacings to hematite species may strongly weaken their magnetic affinity, when compared to the reported magnetic character of hematite nanoparticles in previous works [63,64].

Compared with reference ATT sample, Sp/ATT and Im/ATT clay samples exhibit promising ferromagnetic behavior, where the H_{ci} and M_r values have increased by about 2.5 and 1.1 times, respectively, cf. Table 2. Inspection of literature, the coercivity as well as remanent magnetization are linearly dependent on the morphology of the magnetic materials and their shape anisotropy, for instance, the large non-spherical particles induce higher coercivity and remanent magnetization than small spherical ones [63–65]. From this consideration, the developed magnetic parameters of Sp/ATT and Im/ATT clay samples may possibly attribute to the exfoliating scale in their clay structure and the presence of hematite particles above 10 nm in size, as evidenced by XRD and HR-TEM analyses. These two reasons enhance the magnetic surfaces anisotropy of hematite nanoparticles and prevent them from being magnetized in directions other than along their easy magnetic axes [63], i.e. the Sp/ATT possesses higher H_{ci} and M_r values, larger hematite nanoparticles and much more developed clay-exfoliated system than Im/ATT.

For more clarification to the deep influence of the organo-modifiers on the magnetic affinity of the iron-rich Sinai clay, the squareness is calculated for each clay sample under study and depicted in Table 2. It is worth mentioning that the poor magnetic properties of ATT and Az/ATT are consistent with presence of multi-domain magnetic particles of squareness much <0.1, while the advanced magnetization of Sp/ATT and Im/ATT arise from the single-domain magnetic particles with squareness >0.1 [65,66].

By recalling the DFT calculations of various understudied organoclays, the contribution of HOMO electrons as well the nucleophilic character in terms of gap energy value (ΔE) decreased, according to the organo-modifier used, in the sequence: Az > Im > Sp. These notions verified the potential role of the chemistry of heterocyclic moieties in controlling the stacking order and the various physicochemical characteristics of clay layers, cf. Scheme 1. By considering the above descriptive discussions of physicochemical characteristics of various organoclays, the symmetric and electronic nature of the used organo-modifier are thought to govern the clay interlamellar profile as being expressed in follows: (i) the planar highly nucleophilic Az molecule is promising candidate as an intercalant referring to its ability to percolate into the clay layered structure and underpin repulsion forces between silicate layers, increasing thereby the interlayer spacing (Scheme 1, a), (ii) the non-planar Sp electrophile molecule is preferentially considered as efficient peeling-clay exfoliator regarding to its intimate interaction with negatively charged sites on clay sheets (viz., hydroxyls and bridging oxygens [57]) causing their exfoliation (Scheme 1b), and (iii) the symmetrical Im molecule of electrophilic/nucleophilic nature is being suggested as shear-clay exfoliator resulting from its affinity to interact with various accommodated active sites in clay sheet structure, viz., cation exchangeable sites, Brønsted acid sites, silanols, aluminols, and high adsorption potential surface and edge sites (Scheme 1c) [4,67]. Moreover, the extent of exfoliation scale in Sp/ATT and Im/ATT clay samples most probably emerges hematite nanospheres over the surfaces of clay platelets and encourages their gathering possibilities in contrast to the fully intercalated clay system observed in Az/ATT sample. Such intercalated clay system keen to veil hematite particles within interlayer spacing and render them from being increased in size (Scheme 1).

Besides all of the above-considerations, the organically modified clays understudy are appreciated to be low-cost materials referring to (i) the natural abundance and the ease purification method of bentonite clay, (ii) the low price of chalcone (the main precursor in synthesis of O, N, S heterocyclic compounds, Fig. 1), which is an important constituent in many natural sources like fruits, spices and vegetables [45], and (iii) the simple and cheap procedures applied to synthesis of heterocyclic compounds, where conventional ultrasonic and microwave treatment are required.

3.3. Applicability of understudied magnetized organoclays in lubricating oil field industry

Beyond the reach of controlling the lamellar structure of clay by the chemistry of the heterocyclic organo-modifier, a new enthusiastic step can be brought through applying these organoclays in lubricating oil-field industry as given below.

3.3.1. Enhancement of electrical, physicochemical and lubricant properties of base oil by the understudied organoclay additives

Out of the science box literacy, the enhancing affinity of the various organoclays toward the electrical nature of base oil is judiciously investigated in terms of demonstrating the current-voltage relationship using salinometer device (Fig. 6a) and detecting the electrical

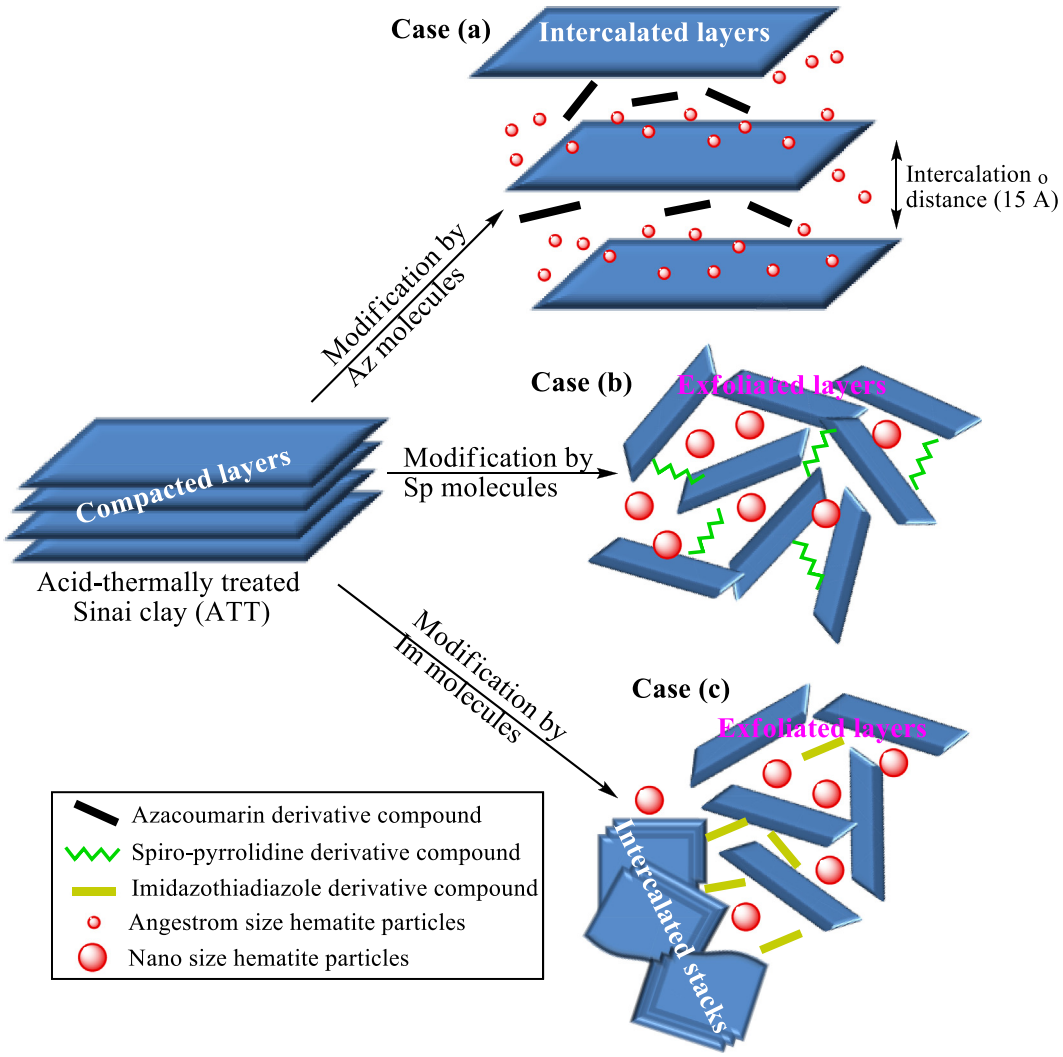

Scheme 1. Schematic illustration represents the interplay between the chemistry of organic modifier and the clay layered structure: (a) fully intercalated, (b) fully exfoliated and (c) partially intercalated/exfoliated clay systems induced by azacoumarin, spiro-pyrrolidine and imidazothiadiazole heterocyclic substituents, respectively.

stimulation efficiencies (ESE, %), Fig. 6b. The results obviously show the propensity of Im/ATT and Sp/ATT organoclay additives to enhance the electrical nature of base oil achieving efficiencies of 125% and 164%, respectively.

Regarding DFT studies and physicochemical properties of both samples, such results most probably refer to the electrophilic character of Im and Sp molecules that instigates interaction with clay layers upgrading their potential and exfoliation extents. To ensure ineffectiveness of Im/ATT and Sp/ATT organoclay additives onto the physicochemical properties of base oil, the flash and pour points as well TAN values of such oil and the base-oil suspensions containing these organoclays are assessed, Fig. 6(c, d and e). The physicochemical characteristics of base oil are shown to be less affected by addition of Sp/ATT; a behavior that perhaps resulted from possession of Sp/ATT to higher surface potential and magnetic characters ($\zeta_{av} = -22.6$ mV and $H_{ci} = 208$ O_e), lower hydrodynamic particle size (~100 nm) and fully exfoliated clay system rather than those exhibited by Im/ATT.

As looking for environmentally friendly base oil lubricant additives becomes of prime importance in scientific community [35,68,69], the friction coefficients and wear scare diameters of the base oil and the base-oil suspension containing Sp/ATT are ruled out and presented in Fig. 7, a and b. The 5 W/40 engine oil is used as reference lubricant oil for a comparison purpose. The friction coefficient and WSD of the base-oil suspension containing Sp/ATT are clearly depressed compared to those of base oil (from 0.17 to 0.04, and from 550 μm to 220 μm, respectively), exhibiting lubrication characteristics close to those of 5 W/40 engine oil (Fig. 7, a and b). Such improvements in friction-reducing and anti-wear properties of base oil lubricated by Sp/ATT additive are most probable regarded to nano-sized dimension, and elevated zeta-potential and magnetic properties of such additive, as evidenced by several previous works [68,69].

3.3.2. Regeneration of waste lubricant oil

The physicochemical properties of engine oil (5 W-40), waste lubricant oil and regenerated oils treated by various understudied organoclays are reported in Table 3. In the comparison of physicochemical properties of waste lubricant oil with those of engine oil, increasing in the density and kinematic viscosity and TAN values are observed for waste oil linked with remarkable declining in the viscosity index, flash point and pour point values, see Table 3. This significant fluctuation in the technical characteristics of waste oil seems to be attributable to the presence of heavy metals and suspensions of undesirable oxidized and polymerized species, viz. organic halogens, carbonyl compounds, polychlorinated biphenyls, etc., in the oil moiety [54,55,68]. As can be seen from Table 3, the technical characteristic of waste lubricant oil is highly improved by treating with Im/ATT clay sample, forming a regenerated oil that satisfies the standard requirements of 5 W/40 engine oil. Moreover, the UV–Visible absorbance peaks in the 430–700 nm region

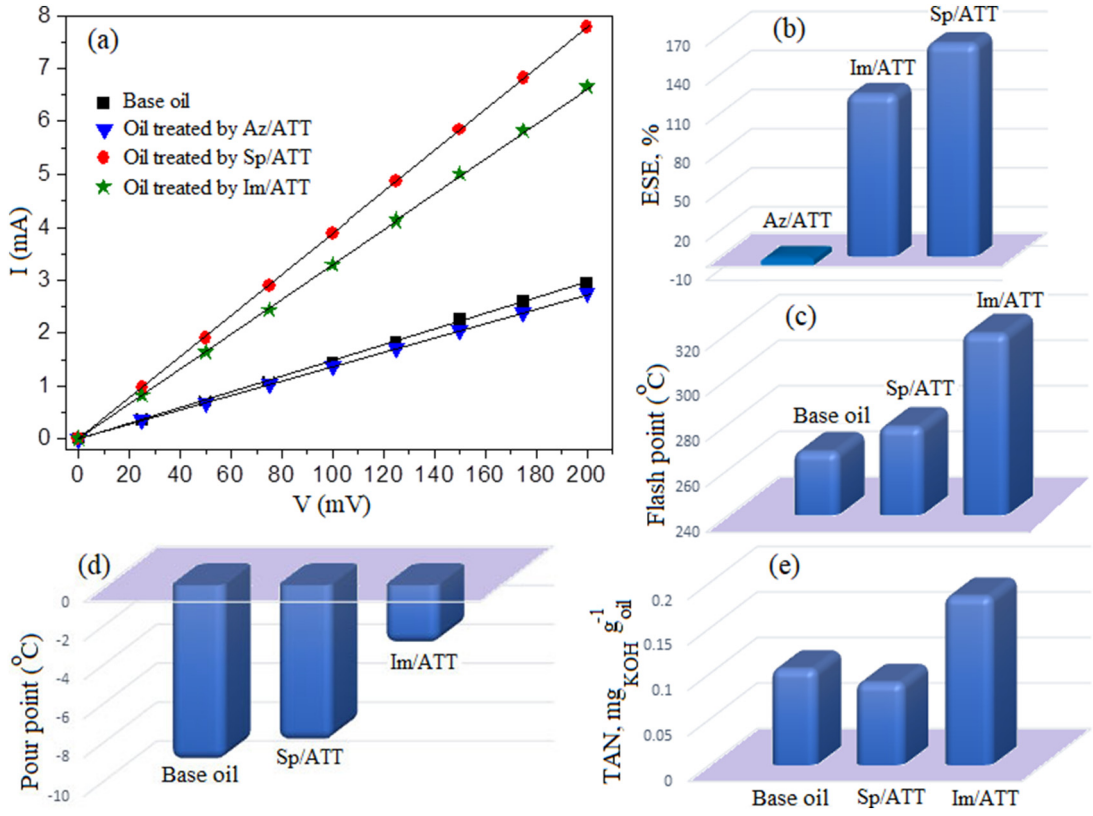

Fig. 6. (a) Current-voltage plots of base oil and oil treated by various organoclay additives, (b) stimulating efficiencies of various organoclays toward electrical property of base oil, and (c), (d) and (e) are the flash points, pour points and total acid numbers physicochemical properties of the base oil and the oil treated by various organoclay additives, respectively.

for the waste oil, the regenerated oils by various organoclay samples and the 5 W-40 engine oil are obtained and represented in Fig. 7c. It is clearly obvious that the dark color of waste oil (of maximum absorbance at $\lambda_{max} = 537$ nm) is radically changed to reddish-brown color for the regenerated oils by Az/ATT and Sp/ATT, as being evidenced from the blue shifting of their λ_{max} to 530 nm and 512 nm, respectively, see Fig. 7c and Table 3. Meanwhile, the color of the regenerated oil by Im/ATT is much brighter and has a clear reddish-yellow color of maximum

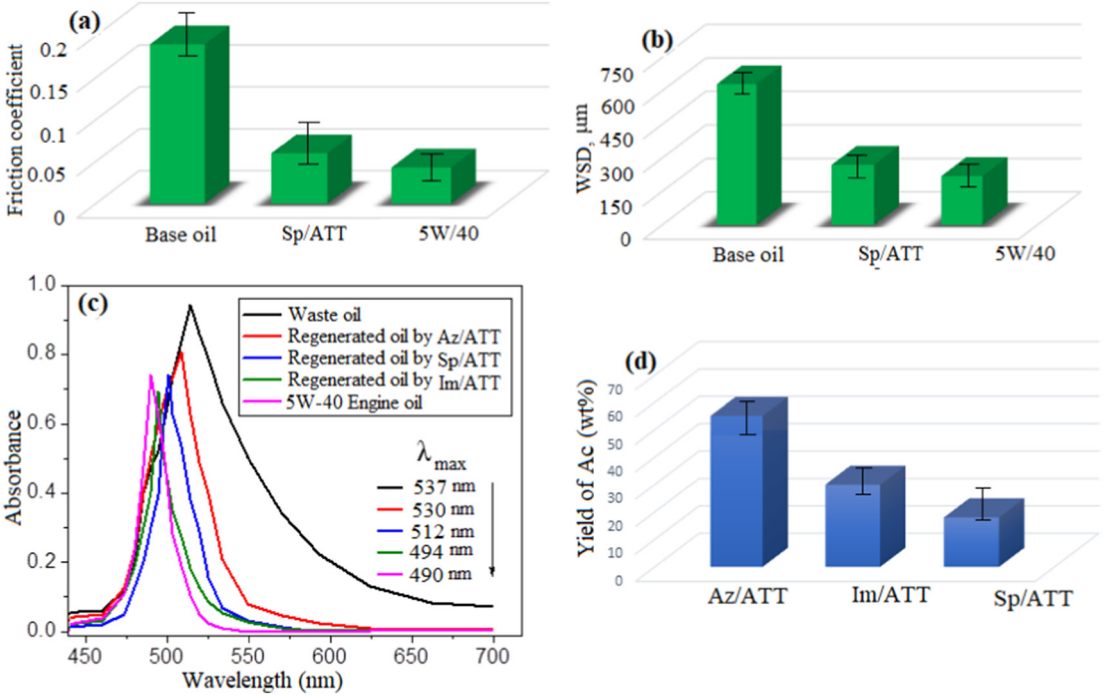

Fig. 7. (a) Friction coefficients and (b) wear scar diameters of base oil, 5 W/40 engine oil and base oil suspension containing Sp/ATT organoclay, (c) the UV absorbance of oils understudy, and (d) catalytic activity of various understudied organoclays toward acetic acid production.

Table 3
Comparison of physicochemical properties of engine oil (5 W-40) with waste lubricant oil and regenerated oils treated by various organoclays.

Physicochemical property	Engine oil (5 W-40)	Waste lubricant oil (after purification)	Regenerated oils after treatment by		
			Az/ATT	Sp/ATT	Im/ATT
Density (g cm^{-3}) at 27.5 °C	0.856	0.924	0.946	0.896	0.836
Kinematic viscosity at 40 °C (cSt)	80.3	192.5	127.3	114.7	82.7
Kinematic viscosity at 100° C (cSt)	13.7	18.8	17.9	16.9	14.1
Viscosity index	175	110	157	161	177
Flash point (°C)	231	102	125	176	232
Pour point (°C)	−9	−15	0	−13	−5
Total acid number (mg KOH/g oil)	0.106	3.851	4.476	1.403	0.087
Oil color					
	Yellow	Graduated colors of reddish-brown			Reddish Yellow

absorbance at a wavelength of 494 nm, complying to the λ_{max} observed by 5 W-40 engine oil, cf. Fig. 7c and Table 3. The unique regenerating affinity of Im/ATT organoclay toward waste lubricant oil is most probable caused by the occurrence of extended diversity in its physical and chemical nature including (i) presence of different pore structure where mesoporous particles are existed exhibiting some microporosity (evidenced from N_2-BET surface analysis), (ii) variance in the lamellar structure of clay as intercalated stacks and exfoliated flacks are randomly distributed in the clay matrix (proved by XRD and HR-TEM analyses) and (iii) abundance of several active sites of various electronic nature either in the clay structure (such as Si-O-Si distorted bridging oxygens, and Si-OH and Al-OH hydroxyls) or in the heterocyclic organic molecule (such as nucleophilic imidazothiadiazole ring and electrophilic naphthalene ring), being demonstrated from DFT and FTIR studies. All such conceptual physicochemical divergences qualify Im/ATT to efficiently interact with coloring matters and other impurities in waste lubricant oil and be a better adsorbent than other studied organoclays. Moreover, the promising recorded magnetic parameters of Im/ATT (see Section 3.2.3) ease from clay separation during oil treatment regeneration process. The adsorption behavior as well the adsorbent content ratio of such organoclay in the regeneration of waste oil will hopefully be addressed in a future publication.

A comparison of the physicochemical characteristics of recycled waste oil using different regenerating agents is listed in Table 4. It is clearly evident that the physicochemical characteristics of the recycled waste oil by most of the used regenerating agents in literature [31,54,55,70–73] were roughly coincide with the requirements needed for engine oil, lacking the latest standards of the oil industry and vehicle manufacturers [74]. For instance, the viscosity indices, pour points and flash points of the regenerated oils obtained from several previous works recorded lower values rather than those registered by 5 W-40 engine oil, see Tables 3 and 4. By considering our results in Tables 3 and 4, Im/ATT organoclay significantly overtops all the existed oil-regeneration agents in literature via producing a regenerated oil of physicochemical characteristics closely matched to those of fresh engine oil.

3.3.3. Production of acetic acid from waste lubricant oil

In this section, the catalytic activities of various organoclays toward selective oxidation of waste lubricant oil to acetic acid have been discussed. As seen from Fig. 7d, the yield of acetic acid (%) is most probable hanged by the chemistry of organo-modifiers (as demonstrated from DFT studies) and to what extent they can able to alter the layered structure, and the populating mode and the size of hematite nanoparticles in the clay matrix. In this respect, Az/ATT clay sample shows a great affinity to produce high yield of acetic acid (~45%) from waste oil (Fig. 7d). The obtained concentration of acetic acid is threefold increasing that obtained by fast pyrolysis of biomass in previous work [37]. A fact that is strongly related to the ability of Az molecules not only to customize a fully intercalated clay structure, but also to acquire populations of angstrom-sized hematite particles within the clay interlayer spacings, as evidenced from XRD and HR-TEM studies. In this respect, for Az/ATT catalyst, the clay intercalation spacings (of ~20 Å) may possibly be emerged not only as nanoreactors but as efficient hostage to the hematite species, which candidate as active centers in the production of acetic acid from waste oil. This finding thus provides a sound basis for further in-depth studies for the effect of catalyst concentration, reaction temperature and reaction time on the yield of acetic acid.

4. Conclusions

A bright future for iron-rich montmorillonite clay from Sinai was introduced in lubricant-oilfield applications through its chemical modification by novel heterocyclic organic compounds like azacoumarin (Az), spiropyrrolidine (Sp) and imidazothiadiazole (Im) substituents. The structure and electronic characteristics of these heterocyclic compounds were investigated by elemental analysis, spectroscopic analyses, including FT-IR, ^{1}H NMR, ^{13}C NMR and MS, and density functional

Table 4
Comparison of the physicochemical characteristics of recycled waste lubricant oil using different regenerating materials.

Regenerating agents	Physicochemical characteristics of various regenerated oils							
	Density, (g cm^{-3}) at 27.5 °C	Ref.	Viscosity index	Ref	Pour point (°C)	Ref.	Flash point (°C)	Ref.
Thermally activated alumina	0.852	[55]	132	[55]	−3	[55]	215	[55]
Activated bentonite clay by H_2SO_4	0.908	[31]	122	[31]	−2	[31]	170	[31]
1-Butanol/methyl ethyl ketone mixture	0.896	[70]	143	[70]	−1	[70]	155	[70]
Toluene/butanol/methanol mixture	0.881	[54]	140	[54]	3	[54]	224	[54]
CH_3COOH	0.872	[71]	89	[71]	−2	[71]	210	[71]
Resinous compounds/vermiculite	0.877	[72]	156	[72]	−3	[72]	217	[72]
Activated charcoal	0.862	[73]	94	[73]	−2	[73]	180	[73]
Im/ATT organically modified clay	0.836	This study	177	This study	−5	This study	232	This study

theory. The physicochemical characteristics of the organoclays containing hematite particles were examined by several techniques (XRD, FTIR, DLS, HR-TEM and N_2-physisorption). Their magnetic properties were also recognized. For Az/ATT, the planarity and nucleophilicity of Az molecules efficiently enhanced their fulfil intercalation into the clay interlayers affording intercalation distance of ~20 Å in which angstrom-size α-Fe_2O_3 particles (<20 Å) are entirely veiled. This situation weakened the interaction between clay layers resulting in presence of near-neutral mesoporous large-sized clay particles with poor magnetic features. For Sp/ATT, the non-planar and electrophilic nature of Sp molecules enthused them to interact firmly with clay sheets, and peel and degenerate the clay ordered profile, forming micro/mesoporous fully exfoliated clay platelets over which hematite nanospheres (of ~20 nm size) were splattered. The obtained clay system possessed lower-sized and higher negatively charged particles of pronounced magnetic character (with coercivity and remanent magnetisation of 208 O_e and 0.04 emμ g^{-1}, respectively) compared to those of Az/ATT. In case of Im/ATT, the diversity in the nucleophilic as well electrophilic character of the planar Im compound inspired shear action on the clay layered structure, showing randomly distributed intercalated stacks with few exfoliated flakes laden with well-dispersed hematite tiny nanospheres (~12 nm). Such unique model trigger clay particles to owe median physicochemical characteristics to those of Az/ATT and Sp/ATT linked with developed magnetic nature (of coercivity 171 O_e and remanent magnetisation 0.04 emμ g^{-1}).

A new enthusiastic step that brought in this study was implementing such organically-modified clay samples in lubricant oilfield industry. The magnetic Sp/ATT organoclay was emerged as potential lubricant additive in base oil, which reduced friction and wear on steel surfaces, and as an enhancer to the physicochemical and electrical properties of base oil with electrical stimulation efficiency of ~164%. Meanwhile, the magnetic Im/ATT sample was candidate as an efficient, easily-separable regenerating agent to waste lubricant oil, and the Az/ATT was strongly suggested as oxidative catalyst for acetic acid production from waste oil (of ~45% yield). The wealth of this research is opening a window on the futuristic big-benefits of organo-modified iron-rich Sinai clays in lubricant oilfield industry.

Supplementary data to this article can be found online at https://doi.org/10.1016/j.molliq.2019.111006.

References

[1] C.H. Zhou, Q. Zhou, Q.Q. Wu, S. Petit, X.C. Jiang, S.T. Xia, C.S. Li, W.H. Yu, Modification, hybridization and applications of saponite: an overview, Appl. Clay Sci. 168 (2019) 136–154.

[2] H. Bu, P. Yuan, H. Liu, D. Liu, J. Liu, et al., Effects of complexation between organic matter (OM) and clay mineral on OM pyrolysis, Geochim. Cosmochim. Acta 212 (2017) 1–15.

[3] F.E.A. Bayaumy, A.S. Darwish, Exfoliated Egyptian kaolin immobilized heteropolyoxotungstate nanocomposite as an innovative antischistosomal agent: *In vivo* and *in vitro* bioactive studies, Mater. Sci. Eng. C 59 (2016) 717–730.

[4] S.A. Hassan, F.Z. Yehia, H.A. Hassan, S.A. Sadek, A.S. Darwish, Various characteristics and catalytic performance of iron (II) phthalocyanine immobilized onto titania- and vanadia-pillared bentonite clay in *in situ* polymerization of methyl methacrylate. An attempt to synthesize novel polymer/iron phthalocyanine/pillared clay nanocomposites, J. Mol. Catal. A 332 (2010) 93–105.

[5] J. Hári1, F. Horváth, J. Móczó, K. Renner, B. Pukánszky, Competitive interactions, structure and properties in polymer/layered silicate nanocomposites, Express Polym Lett 11 (2017) 479 - 492.

[6] A. Kausar, M. Iqbal, A. Javed, K. Aftab, Z. Nazli, H.N. Bhatti, S. Nouren, Dyes adsorption using clay and modified clay: a review, J. Mol. Liq. 256 (2018) 395–407.

[7] S.L. Bee, M.A.A. Abdullah, S.T. Bee, L.T. Sin, A.R. Rahmat, Polymer nanocomposites based on silylated-montmorillonite: a review, Prog. Polym. Sci. 85 (2018) 57–82.

[8] A. De Stefanis, A.A.G. Tomlinson, Towards designing pillared clays for catalysis, Catal. Today 114 (2006) 126–141.

[9] N. Shukla, A.K. Thakur, Ion transport model in exfoliated and intercalated polymer – clay nanocomposites, Solid State Ionics 181 (2010) 921–932.

[10] A. Kausar, M. Iqbal, A. Javed, K. Aftab, Z.H. Nazli, H.N. Bhatti, S. Nouren, Dyes adsorption using clay and modified clay: a review, J. Mol. Liq. 256 (2018) 395–407.

[11] Z. Orolínová, A. Mockovciaková, V. Zelenák, M. Myndyk, Influence of heat treatment on phase transformation of clay–iron oxide composite, J. Alloys Compd. 511 (2012) 63–69.

[12] F.G.E. Nogueira, J.H. Lopes, A.C. Silva, R.M. Lago, J.D. Fabris, L.C.A. Oliveira, Catalysts based on clay and iron oxide for oxidation of toluene, Appl. Clay Sci. 51 (2011) 385–389.

[13] S. Narayanan, K. Deshpande, Alumina pillared montmorillonite: characterization and catalysis of toluene benzylation and aniline ethylation, Appl. Catal. A: General 193 (2000) 17–27.

[14] S. Drouin, M. Boussafir, J.L. Robert, P. Alberic, A. Durand, Carboxylic acid sorption on synthetic clays in sea water: in vitro experiments and implications for organo-clay behaviour under marine conditions, Org. Geochem. 41 (2010) 192–199.

[15] T. Phothitontimongkol, N. Siebers, N. Sukpirom, F. Unob, Preparation and characterization of novel organo-clay minerals for hg(II) ions adsorption from aqueous solution, Appl. Clay Sci. 43 (2009) 343–349.

[16] L.C.A. Oliveira, R.V.R.A. Rios, J.D. Fabris, K. Sapag, V.K. Garg, R.M. Lago, Clay – iron oxide magnetic composites for the adsorption of contaminants in water, Appl. Clay Sci. 22 (2003) 169–177.

[17] F.A. Ngwabebhoh, S.I. Erdagi, U. Yildiz, Pickering emulsions stabilized nanocellulosic-based nanoparticles for coumarin and curcumin nanoencapsulations: in vitro release, anticancer and antimicrobial activities, Carbohydr. Polym. 201 (2018) 317–328.

[18] S. Poojari, P.P. Naik, G. Krishnamurthy, K.S.J. Kumara, N.S. Kumar, S. Naik, Anti-inflammatory, antibacterial and molecular docking studies of novel spiro-piperidine quinazolinone derivatives, J. Taibah Univ. Sci. 11 (2017) 497–511.

[19] B. Chandrakantha, A.M. Isloor, P. Shetty, H.K. Fun, G. Hegde, Synthesis and biological evaluation of novel substituted 1,3,4-thiadiazo le and 2,6-d i aryl substituted imidazo [2,1- b] [1,3,4] thiadiazole derivatives, Eur. J. Med. Chem. 71 (2014) 316–323.

[20] A. Fais, B. Era, S. Asthana, V. Sogos, R. Medda, L. Santana, E. Uriarte, M.J. Matos, F. Delogu, A. Kumar, Coumarin derivatives as promising xanthine oxidase inhibitors, Intern J. Biol. Macromolec 120 (2018) 1286–1293.

[21] K.S. Mani, B. Murugesapandian, W. Kaminsky, S.P. Rajendran, Enantioselective approach towards the synthesis of spiro-indeno [1,2- b] quinoxaline pyrrolothiazoles as antioxidant and antiproliferative, Tetrahedron Lett. 59 (2018) 2921–2929.

[22] V.B. Jadhav, M.V. Kulkarni, V.P. Rasal, S.S. Biradar, M.D. Vinay, Synthesis and anti-inflammatory evaluation of methylene bridged benzofuranyl imidazo [2,1-b] [1,3,4] thiadiazoles, Eur. J. Med. Chem. 43 (2008) 1721–1729.

[23] M.A. Ali, R. Ismail, T.S. Choon, Y.K. Yoon, A.C. Wei, S. Pandian, R.S. Kumar, H. Osman, E. Manogaran, Substituted spiro [2.3′] oxindolespiro [3.2″]-5,6-dimethoxy-indane-1″-one-pyrrolidine analogue as inhibitors of acetylcholinesterase, Bioorg. Med. Chem. Lett. 20 (2010) 7064–7066.

[24] S.S. Karki, K. Panjamurthy, S. Kumar, M. Nambiar, S.A. Ramareddy, K.K. Chiruvella, S.C. Raghavan, Synthesis and biological evaluation of novel 2-aralkyl-5-substituted-6-(4 0 -fluorophenyl)-imidazo [2,1-b][1,3,4]thiadiazole derivatives as potent anticancer agents, Eur. J. Med. Chem. 46 (2011) 2109–2116.

[25] H.M. Patel, M.N. Noolvi, N.S. Sethi, A.K. Gadad, S.S. Cameotra, Synthesis and antitubercular evaluation of imidazo [2,1-b][1,3,4] thia diazole derivatives, Arab. J. Chem. 10 (2017) S996–S1002.

[26] H.M. Patel, M.N. Noolvi, A. Goyal, B.S. Thippeswamy, 2,5,6-Trisubstituted imidazo [2,1- b] [1,3,4] thiadiazoles: search for antihyperlipidemic agents, Eur. J. Med. Chem. 65 (2013) 119–133.

[27] M.P.N. Rao, B. Nagaraju, J. Kovvuri, S. Polepalli, S. Alavala, M.V.P.S. Vishnuvardhan, P. Swapna, V.D. Nimbarte, J.K. Lakshmi, N. Jain, A. Kamal, Synthesis of imidazo-thiadiazole linked indolinone conjugates and evaluated their microtubule network disrupting and apoptosis inducing ability, Bioorg. Chem. 76 (2018) 420–436.

[28] C. Salgado, M.P. Arrieta, L. Peponi, D. López, M.F. García, Photo-crosslinkable polyurethanes reinforced with coumarin modified silica nanoparticles for photo-responsive coatings, Prog. Org. Coating 123 (2018) 63–74.

[29] R. Najjar, E. Bigdeli, Synthesis of novel core-shells of PMMA with coumarin based liquid crystalline side chains and PMMA shell as electro-optical materials, Eur. Polym. J. 104 (2018) 136–146.

[30] M.C. Sil, M.F.M. Kavungathodi, J. Nithyanandhan, Effect and position of spiro-bipropylenedioxythiophene π-spacer in donor- π-spacer-acceptor dyes for dye-sensitized solar cell, Dyes Pigments 161 (2019) 313–323.

[31] S. Salem, A. Salem, A.A. Babaei, Application of Iranian nano-porous Ca-bentonite for recovery of waste lubricant oil by distillation and adsorption techniques, J. Ind. Eng. Chem. 23 (2015) 154–162.

[32] S. Shahnazar, S. Bagheri, S.B. Abd Hamid, Enhancing lubricant properties by nanoparticle additives, Int. J. Hydrorg. Energy 41 (2016) 3153–3170.

[33] K. Holmberg, P. Andersson, N.O. Nylund, K. Mäkelä, A. Erdemir, Global energy consumption due to friction in trucks and buses, Tribol. Int. 7 ((2014) 94–114.

[34] S.N.A. Ramlan, W.J. Basirun, S.W. Phang, D.T.C. Ang, Electrically conductive palm oil-based coating with UV curing ability, Prog. Org. Coating 112 (2017) 9–17.

[35] R. Gusain, O.P. Khatri, Fatty acid ionic liquids as environmentally friendly lubricants for low friction and wear, RSC Adv. 6 (2016) 3462–3469.

[36] A.J. Jafari, M. Hassanpour, Analysis and comparison of used lubricants, regenerative technologies in the world, Resour. Conserv. Recy. 103 (2015) 179–191.

[37] S.J. Oh, G.G. Choi, J.S. Kim, Production of acetic acid-rich bio-oils from the fast pyrolysis of biomass and synthesis of calcium magnesium acetate deicer, J. Anal. Appl. Pyrol 124 (2017) 122–129.

[38] Y.T. Wang, Z. Fang, X.X. Yang, Biodiesel production from high acid value oils with a highly active and stable bifunctional magnetic acid, Appl. Energ. 204 (2017) 702–714.

[39] M. Yan, C. Sun, J. Dong, J. Xu, W. Ke, Electrochemical investigation on steel corrosion in iron-rich clay, Corros. Sci. 97 (2015) 62–73.

[40] A. Ausavasukhi, T. Sooknoi, Catalytic activity enhancement by thermal treatment and re-swelling process of natural containing iron-clay for Fenton oxidation, J. Coll. Interf. Sci. 436 (2014) 37–40.

[41] R.R. Pawar, Lalhmunsiama, M. Kima, J.G. Kim, S.M. Hong, S.Y. Sawant, S.M. Lee, Efficient removal of hazardous lead, cadmium, and arsenic from aqueous environment by iron oxide modified clay-activated carbon composite beads, Appl. Clay Sci. 162 (2018) 339–350.
[42] S.A. Rizk, A.M. El-Naggar, A.A. El-Badawy, Synthesis, spectroscopic characterization and computational chemical study of 5-cyano-2-thiouracil derivatives as potential antimicrobial agents, J. Mol. Struct. 1155 (2018) 720–733.
[43] M.A. El-Hashash, S.A. Rizk, A.A. El-Badawy, Ultrasonic aptitude of Regioselective reaction of 6-bromo-spiro-3,1-benzoxazinone 2,1′-isobenzofuran-3′,4-dione towards some electrophilic and Nucleophilic reagents, J. Heterocyclic Chem. 55 (2018) 2090–2098.
[44] J. Haginaka, Recent progresses in protein-based chiral stationary phases for enantioseparations in liquid chromatography, J. Chromatogr. B 875 (2008) 12–19.
[45] S.A. Rizk, S.S. Abdelwahab, H.A. Sallam, Regioselective reactions, spectroscopic characterization, and cytotoxic evaluation of spiro-pyrrolidine thiophene, J. Heterocyclic Chem. 55 (2018) 1604–1614.
[46] J. Xu, W. Wang, A. Wang, Stable formamide/palygorskite nanostructure hybrid material fortified by high-pressure homogenization, Powder Technol. 318 (2017) 1–7.
[47] K. Khederlou, R. Bagheri, A. Shojaei, A mathematical method for XRD pattern interpretation in clay containing nano composites, Appl. Surf. Sci. 318 (2014) 90–94.
[48] J.H. De Boer, B.C. Lippens, B.G. Linsen, J.C.P. Broekhoff, A. van den Heunel, T.V. Osinga, The t-curve of multimolecular N_2 adsorption, J. Coll. Interf. Sci. 21 (1966) 405–414.
[49] K.W. Sing, D.H. Everett, R.A.W. Haul, L. Moscou, R.A. Pierotti, J. Rouquerol, T. Siemieniewska, Reporting physisorption data for gas/solid systems with special reference to the determination of surface area and porosity, Pure Appl. Chem. 57 (1985) 603–619.
[50] R. Scott, J. Fitch, L. Leugner, The Practical Handbook of Machinery Lubrication, fourth ed. Noria Publ. Comp, USA, 2012.
[51] ASTM, D 3230 – 99, Standard Test Method for Salts in Crude Oil (Electrometric Method), Chapter 7, An American national standard, U.S.A., 2004
[52] ASTM, Annual Book of Standard Petroleum Products and Lubricants, Chapter 5, vol. (05.01-05.03), American society for testing and materials, U.S.A., 2000
[53] IP, Standard Methods for Analysis and Testing of Petroleum and Related Products, The institute of petroleum, London, U.K, 1999.
[54] D.I. Osman, S.K. Attia, A.R. Taman, Recycling of used engine oil by different solvent, Egypt. J. Petrol. 27 (2018) 221–225.
[55] A.E. Elsayed, S.K. Atya, D.I. Osman, M.F. Amin, E.M. Shoukry, A.R. Taman, Production of virigin lubricating oil from used engine using solvent extraction and adsorption process, Int. J. Novel Res. Phys. Chem. mathematics 3 (2016) 13–17.
[56] F. El-Taib Heakal, S.A. Rizk, A.E. Elkholy, Characterization of newly synthesized pyrimidine derivatives for corrosion inhibition as inferred from computational chemical analysis, J. Mol. Struct. 1152 (2018) 328–336.
[57] S.A. Hassan, A.S. Darwish, H.M. Gobara, N.E.A. Abed-elsatar, S.R. Fouda, Interaction profiles in poly (amidoamine) dendrimer/montmorillonite or rice straw ash hybrids-immobilized magnetite nanoparticles governing their removal efficiencies of various pollutants in wastewater, J. Mol. Liq. 230 (2017) 353–369.
[58] A. Rufus, N. Sreeju, V. Vilas, D. Philip, Biosynthesis of hematite (α-Fe_2O_3) nanostructures: size effects on applications in thermal conductivity, catalysis, and antibacterial activity, J. Mol. Liq. 242 (2017) 537–549.
[59] B.D. Cullity, S.R. Stock, Elements of X -Ray Diffraction, third ed. Addison–Wesley, Massachusetts, 2001.
[60] A.J. Bur, Y.H. Lee, S.C. Roth, P.R. Start, Measuring the extent of exfoliation in polymer/clay nanocomposites using real-time process monitoring methods, Polymer 46 (2005) 10908–10918.
[61] H.R. Dennis, D.L. Hunter, D. Chang, S. Kim, J.L. White, J.W. Cho, D.R. Paul, Effect of melt processing conditions on the extent of exfoliation in organoclay-based nanocomposites, Polymer 42 (2001) 9513–9522.
[62] N.N. Bhiwankar, R.A. Weiss, Melt intercalation/exfoliation of polystyrene-sodium-montmorillonite nanocomposites using sulfonated polystyrene ionomer compatibilizers, Polymer 47 (2006) 6684–6691.
[63] F. Song, J. Guan, X. Fan, G. Yan, Single-crystal star-like arrayed particles of hematite: synthesis, formation mechanism and magnetic properties, J. Alloys Compd. 485 (2009) 753–758.
[64] L. Bao, H. Yang, X. Wang, F. Zhang, R. Shi, B. Liu, L. Wang, H. Zhao, Synthesis and size-dependent magnetic properties of single-crystalline hematite nanodiscs, J. Cryst. Growth 328 (2011) 62–69.
[65] B. Alqasem, N. Yahya, S. Qureshi, M. Irfan, Z.U. Rehman, H. Soleimani, The enhancement of the magnetic properties of α -Fe_2O_3 nanocatalyst using an external magnetic field for the production of green ammonia, Mater. Sci. Eng. B 217 (2017) 49–62.
[66] H. Shokrollahi, A review of the magnetic properties, synthesis methods and applications of maghemite, J. Magn. Magn. Mater. 426 (2017) 74–81.
[67] M.A. Mekewi, A.S. Darwish, M.E. Amin, H.A. Bourazan, Sustainable removal of Cu^{2+}, Ni^{2+} and Zn^{2+} ions from severe contaminated water using kaolin/poly(glycine) composites, characterization and uptake studies, Desalin. Water Treat. 51 (2013) 7746–7763.
[68] R. Gusain, R. Singh, K.L.N. Sivakumar, O.P. Khatri, Halogen-free imidazolium/ammonium-bis(salicylato)borate ionic liquids as high performance lubricant additives, RSC Adv. 4 (2014) 1293–1301.
[69] A.F. Yetim, H. Kovacı, M. Aslan, A. Çelik, The effect of magnetic field on the wear properties of a ferromagnetic steel, Wear 301 (2013) 636–640.
[70] C.T. Pinheiro, R.F. Pais, M.J. Quina, L.M.G. Ferreira, Regeneration of waste lubricant oil with distinct properties by extraction-flocculation using green solvents, J. Clean. Prod. 200 (2018) 578–587.
[71] I. Hamawand, T. Yusaf, S. Rafat, Recycling of waste engine oils using a new washing agent, Energies 6 (2013) 1023–1049.
[72] K.K. Syrmanova, A.Y. Kovaleva, Z.B. Kaldybekova, N.Y. Botabayev, Y.T. Botashev, B.Y. Beloborodov, Chemistry and recycling Technology of Used Motor oil, Orient. J. Chem. 33 (2017) 3195–3199.
[73] J.D. Udonne, A comparative study of recycling of used lubrication oils using distillation, acid and activated charcoal with clay methods, J. Petroleum Gas Eng. 2 (2011) 12–19.
[74] API, American Petroleum Institute, Lubricating Oils & Greases, API Publishing services, Washington, USA, 2019.